Impact of Storm-Scale Lightning Data Assimilation on WRF-ARW Precipitation Forecasts during the 2013 Warm Season over the Contiguous United States

ALEXANDRE O. FIERRO AND ADAM J. CLARK

Cooperative Institute for Mesoscale Meteorological Studies, University of Oklahoma, and NOAA/OAR/National Severe Storms Laboratory, Norman, Oklahoma

EDWARD R. MANSELL AND DONALD R. MACGORMAN

NOAA/National Severe Storms Laboratory, Norman, Oklahoma

SCOTT R. DEMBEK

Cooperative Institute for Mesoscale Meteorological Studies, University of Oklahoma, Norman, Oklahoma

CONRAD L. ZIEGLER

NOAA/National Severe Storms Laboratory, Norman, Oklahoma

(Manuscript received 3 June 2014, in final form 24 October 2014)

ABSTRACT

This work evaluates the performance of a recently developed cloud-scale lightning data assimilation technique implemented within the Weather Research and Forecasting Model running at convection-allowing scales (4-km grid spacing). Data provided by the Earth Networks Total Lightning Network for the contiguous United States (CONUS) were assimilated in real time over 67 days spanning the 2013 warm season (May–July). The lightning data were assimilated during the first 2 h of simulations each day. Bias-corrected, neighborhood-based, equitable threat scores (BC-ETSs) were the chief metric used to quantify the skill of the forecasts utilizing this assimilation scheme. Owing to inferior observational data quality over mountainous terrain, this evaluation focused on the eastern two-thirds of the United States.

During the first 3 h following the assimilation (i.e., 3-h forecasts), all the simulations suffered from a high wet bias in forecasted accumulated precipitation (APCP), particularly for the lightning assimilation run (LIGHT). Forecasts produced by LIGHT, however, had a noticeable, statistically significant ($\alpha = 0.05$) improvement over those by the control run (CTRL) up to 6 h into the forecast with BC-ETS differences often exceeding 0.4. This improvement was seen independently of the APCP threshold (ranging from 2.5 to 50 mm) and the neighborhood radius (ranging from 0 to 40 km) selected. Past 6 h of the forecast, the APCP fields from LIGHT progressively converged to that of CTRL probably due to the longer-term evolution being bounded by the large-scale model environment. Thus, this computationally inexpensive lightning assimilation scheme shows considerable promise for routinely improving short-term ($\leq$6 h) forecasts of high-impact weather by convection-allowing forecast models.

1. Introduction

The numerical prediction of deep, moist convection remains a challenging problem owing to complex physical interactions between dynamical and microphysical processes over a large range of scales that must be reasonably well depicted by the model (e.g., Bryan et al. 2003; Weisman et al. 2008; Fierro et al. 2009; Kain et al. 2010a). The difficulties associated with convective-scale numerical weather prediction (NWP) are particularly evident at the ''convection allowing'' spatial scales typified by grid spacings on the order of 2–4 km that correspond to minimum resolvable wavelengths of

Corresponding author address: Alexandre O. Fierro, CIMMS, National Weather Center, Suite 2100, 120 David L. Boren Blvd., Norman, OK 73072.
E-mail: alex.fierro@noaa.gov

DOI: 10.1175/MWR-D-14-00183.1

© 2015 American Meteorological Society

12–24 km (e.g., Weisman et al. 2008; Clark et al. 2010a,b; Kain et al. 2010b).

Several recent studies have highlighted that convection-allowing forecasts were able to better predict the frequency and mode of convection, particularly mesoscale convective systems (MCSs) and supercells, than coarser forecasts using convection parameterization (e.g., Done et al. 2004; Kain et al. 2006, 2008; Weisman et al. 2008; Dixon et al. 2009; Clark et al. 2010a). Along the same lines, Ikeda et al. (2013) demonstrated that the High-Resolution Rapid Refresh (HRRR) model was able to reliably predict the timing and location of areas of ground-accumulated snow, rain, and mixed-phase precipitation. These studies all emphasized that higher-resolution grids provide more relevant information on the morphology, evolution, and initiation of the convection. Owing to these notable improvements, many research and operational centers have recently implemented convection-allowing model configurations (Clark et al. 2007; Weisman et al. 2008; Stensrud et al. 2009; Coniglio et al. 2010; Schwartz et al. 2010; Baldauf et al. 2011; Kain et al. 2008, 2010a,b, 2013; Ikeda et al. 2013).

Conventional data sources for the large-scale fields utilized to derive initial and lateral boundary conditions of the convection-allowing forecasts, however, typically exist on coarser grids (e.g., Kain et al. 2010a; Clark et al. 2010b). Thus, the model is forced to "spin up" incipient cell-scale circulations (e.g., convective overturning) during the first 3–6 h of the simulation (Skamarock 2004). To alleviate this problem, it has become attractive to seek computationally efficient approaches aimed at assimilating observational datasets that are of the same order of scale of the model grid (e.g., radar data; Zhang et al. 2009; Aksoy et al. 2009; Dixon et al. 2009; Kain et al. 2010a; Gao and Stensrud 2012; Gao et al. 2013). As described in this work, one possible source of data that could be utilized to achieve this goal is lightning.

This study focuses on evaluating the performance of forecasted accumulated precipitation (APCP) using a recently developed computationally inexpensive lightning data nudging method (Fierro et al. 2012, hereafter F12), which utilizes observed two-dimensional gridded total lightning flash rate density as the main input variable.

In contrast to the relatively large number of studies that have explored assimilation of conventional radar data into NWP models, comparatively few have focused their attention on the assimilation of lightning data (Alexander et al. 1999; Chang et al. 2001; Benjamin et al. 2004; Papadopoulos et al. 2005; Mansell et al. 2007; Pessi and Businger 2009; F12; Fierro et al. 2014, hereafter F14; Marchand and Fuelberg 2014; Mansell 2014). In comparison to the above listed lightning assimilation works, the assimilation of radar data is conventionally achieved through more sophisticated and computationally expensive techniques such as (i) variational codes such as 3DVAR (e.g., Gao and Stensrud 2012) or (ii) ensemble techniques such as the ensemble Kalman filter (EnKF, e.g., Evensen 1994, 2003; Houtekamer and Mitchell 1998; Zhang et al. 2009; Aksoy et al. 2009; Godinez et al. 2012). A review on recent lightning data assimilation studies is provided in F12 and F14 and the reader is invited to consult these manuscripts for details. In summary, these studies highlight the potential benefit of assimilating total lightning data toward improving the analysis and short-term forecast of high-impact weather ranging from the mesoscale (e.g., Mansell et al. 2007) to the storm scale (F12).

One chief motivation for an increasing systematic use of lightning data assimilation is the forthcoming first launch of the Geostationary Operational Environmental Satellite "R" series (GOES-R; Gurka et al. 2006; Goodman et al. 2012, 2013) in 2016. The GOES-R will be equipped with the Geostationary Lightning Mapper (GLM; Goodman et al. 2013) that will be capable of mapping total lightning [intracloud (IC) and cloud-to-ground (CG) flashes] day and night, year-round with a nearly uniform resolution over the Americas ranging between 8 and 12 km (Gurka et al. 2006). In contrast to conventionally assimilated weather surveillance radar data, lightning detected by satellite does not suffer from poor coverage in mountainous areas and oceans. Moreover, unlike satellite-based detection methods, current ground-based networks are less able to detect and locate lower-amplitude sferics from IC flashes, which account for the vast majority of the total flashes (IC:CG ratio near 2:1; Boccippio et al. 2001) with IC:CG ratios nearing 10:1 within severe deep continental storms (e.g., MacGorman et al. 1989). This limitation is critical given that in contrast to CG flashes, IC flash rates were shown to better correlate with updraft development and evolution (e.g., MacGorman et al. 1989; Wiens et al. 2005; Fierro et al. 2006, 2011; Deierling and Petersen 2008). Hence, it is expected that the assimilation of total lightning data would serve as a better proxy (compared to CG alone) toward improving the placement and evolution of high-impact weather at the analysis time.

2. Model setup and assimilation procedure

The numerical model employed in this study is the three-dimensional compressible nonhydrostatic Weather Research and Forecasting (WRF) Model with the Advanced Research WRF (ARW) dynamic solver (WRF-ARW, version 3.4.1) developed by the National Center of Atmospheric Research (Skamarock and Klemp 2008).

a. Model grid configuration and physics options

The physics parameterizations and large-scale fields necessary for providing the initial and boundary

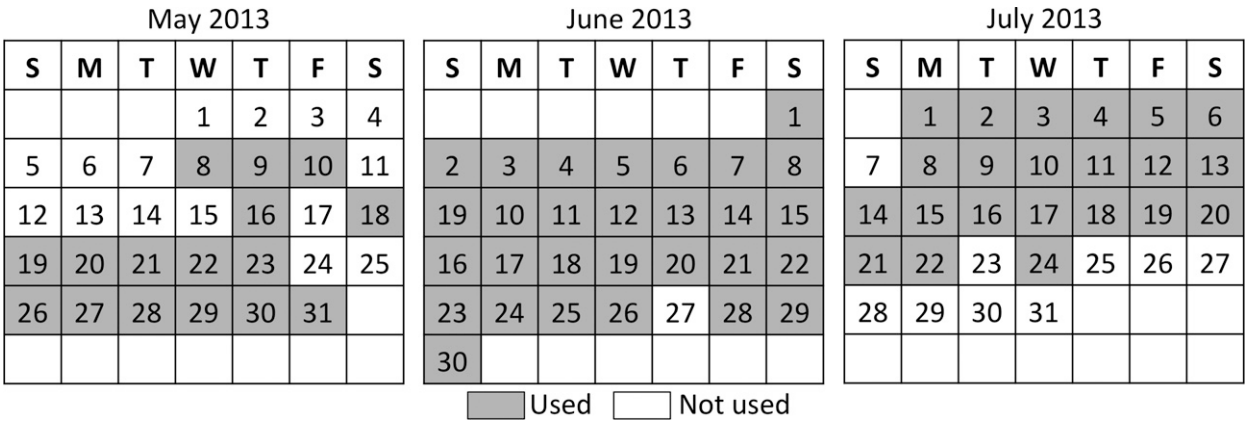

FIG. 1. May–July 2013 calendar highlighting the cases that were used (gray shaded) and not used (white) in this study.

conditions are identical to that of the National Severe Storms Laboratory's (NSSL) daily experimental forecast runs over the contiguous United States (CONUS; Kain et al. 2010b) known as the NSSL-WRF. The NSSL-WRF provides guidance to Storm Prediction Center forecasters and serves as a testing ground for the development of storm-scale model diagnostics (Clark et al. 2007, 2010b; Kain et al. 2010a). The main physics options are the WRF single-moment 6-class bulk microphysics scheme from Hong and Lim (2006), the Mellor–Yamada–Janjic "Eta" turbulence kinetic energy scheme for the boundary layer (Mellor and Yamada 1982; Janjic 1994) with Monin–Obukhov–Janjic similarity theory for subgrid-scale turbulence (Chen et al. 1997), the unified Noah land surface model (Chen and Dudhia 2001; Ek et al. 2003), and the Dudhia (1989) shortwave and Rapid Radiative Transfer Model (RRTM) longwave radiation (Mlawer et al. 1997) schemes. No cumulus parameterization is employed. For each of the 67 forecast days spanning the 2013 warm season (May–July, Fig. 1), forecasts were initialized at 0000 UTC and integrated 24 h (in lieu of 36 h in NSSL-WRF). The initial and boundary conditions were derived from the 3-hourly North American Mesoscale Model (NAM) 40-km grid-spacing analyses and forecasts, respectively. As can be noted in Fig. 1, forecast on several days were not available owing to technical problems encountered during the course of this experiment, including network outages, node failure, unavailability of some of the input data at runtime, or system reboot and maintenance. Because the 0000 UTC NAM data are delivered at about 0300 UTC daily, the NSSL-WRF lightning assimilation runs were started at 0415 UTC. The lightning data, on the other hand, are disseminated almost in real time, and so introduced no additional lag themselves. All simulations employed 128 cores with the assimilation of lightning requiring relatively little additional computational time (i.e., <5 min) to the 3.5 h already necessary to complete a 24-h forecast. With this set up, it took 5 h of simulation "forecast" time, which included the lightning assimilation period (see section 2b below), to "catch up" to the actual local time. In other words, starting at 0415 UTC, the WRF runs with lightning assimilation integrated to 0500 UTC when the actual time was 0500 UTC and integrated to 0000 UTC the next day (i.e., the 24-h forecast) when the actual time was 0745 UTC, 3.5 h after the run began.

The simulation domain (Fig. 2) has a uniform horizontal grid spacing of 4 km and horizontal dimensions in grid points of 1200 × 800. The stretched vertical grid has 35 levels with the model top set at 50 hPa (~20 km). The computational time step is 24 s. For each of the 67 forecast days in Fig. 1, the forecast with the assimilation of total lightning (referred to as LIGHT, see section 2b) was performed in tandem with a control simulation (CTRL) where no data were assimilated. The model data were saved every hour during the 24-h simulation period.

The simulated APCP fields were evaluated against the National Centers for Environmental Prediction's stage-IV multisensor hourly rainfall accumulation estimates

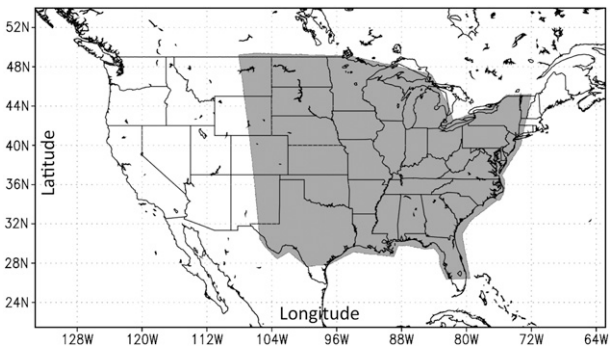

FIG. 2. Sketch of the WRF-NSSL simulation domain (4-km grid spacing) with the gray-shaded area (or mask) indicating the subdomain where the analysis was performed.

(Baldwin and Mitchell 1997) made publicly available by the Earth Observing Laboratory (http://data.eol.ucar.edu). Despite currently being the best observational dataset of this kind, it does suffer from several limitations including radars being out of calibration, rain gauges being clogged, and partial beam blockages due to buildings and terrain. Owing to radar beam blockage induced by terrain, only data covering the eastern two-thirds of the United States were considered for this analysis (see Fig. 2). To compare model and observations, the hourly stage-IV data were remapped from its native 4-km polar stereographic grid onto the WRF 4-km Lambert conformal grid (Fig. 2).

b. *Summary of the lightning data assimilation procedures*

The details behind the lightning data assimilation procedures can be found in F12 and F14 and, hence, are only briefly reviewed here. The lightning data used in this work are provided by the Earth Networks Total Lightning Network (ENTLN). Their network detects both IC and CG flashes with a national-average detection efficiency exceeding 95% for typical CG return strokes and about 50% for typical IC flashes. The location accuracy of ENTLN varies from tens of meters in dense areas of the network to about 500 m elsewhere (see Fig. 6 in F12).

At observed lightning locations, the cloud-scale lightning assimilation imposes incremental increases in water vapor mixing ratio (q_v) within the mixed-phase layer (between 0° and −20°C) wherein electrification processes (i.e., noninductive charging) were shown to be most active (e.g., Takahashi 1978; Saunders and Peck 1998; Emersic and Saunders 2010; Bruning et al. 2010; Fierro et al. 2013). Based on a recent study from Marchand and Fuelberg (2014), it is possible that increasing water vapor within a layer confined in the lower troposphere (below ~700 hPa) instead of the mixed-phase region would allow convection to become more quickly rooted in the boundary layer and, incidentally, allow the present scheme to potentially better represent weakly forced deep convection. The nudging-induced increase in q_v at a grid point within this layer is proportional to the observed gridded total flash rate density (per 4-km grid cell herein). To impose minimal constraints on the running model, two conditionals were devised: (i) the q_v increase is inversely proportional to the simulated graupel mixing ratio (q_g) with zero nudging applied at q_g exceeding 2 g kg^{-1} and (ii) increases in q_v are only applied at lightning locations with a simulated relative humidity (RH) ≤95% (with respect to liquid water). In other words, the aforementioned conditionals do not nudge the layer toward saturation if the conditions within the model already are indicative of the presence of convection (through q_g) or nearly saturated already. Nudging over a confined layer further reduces the total water mass introduced by the assimilation.

The present simulations employ the same nudging coefficients B, C, and D as in F12 [see their Eq. (1) and their Fig. 7][1] and F14 as these were specifically designed for convection-allowing scales. Some differences should be noted, however. First, F12 used a lower RH threshold [coefficient A in their Eq. (1)] because the nudging was simultaneously applied on three grids, namely a 9-km parent grid containing two nested grids with a horizontal grid spacing of 3 and 1 km, respectively. Because the convective response to the assimilation of lightning increased as the grid spacing decreased (F12), the RH threshold needed to be lowered from 95% to ~80% (i.e., the grid volume where nudging is applied decreased) to avoid potential mass–wind imbalance on the 1-km grid, as noted in their study. The authors take this opportunity to point out that F14 used $A = 95\%$, not 80% as stated in that study. Another difference is the use of a lower q_g threshold (2 g kg^{-1}) than in the two aforementioned studies (which used 3 g kg^{-1}). A lower threshold was chosen because instances of RH < 95% and q_g exceeding either 3 or 2 g kg^{-1} remain relatively rare in the model. Thus, in principle, similar results can be achieved using a lower q_g threshold.

It is relevant to reiterate that this simple lightning assimilation technique does not address the development of spurious convection arising from errors in the model and in the initial conditions (F12; F14). While forcing convection at the observed lightning locations through incremental increases of water vapor mass is conceptually succinct, the removal of spurious convection in a balanced manner remains a far more difficult problem.

To reasonably resolve storm motion, the lightning data for each day were binned into 10-min intervals and assimilated during the first 2 h of the simulations, namely between 0000 and 0200 UTC. By virtue of this set up, the forecasts thus start at 0200 UTC. The nudging of water vapor is maintained throughout the 10-min interval at each computational time step until switching to the next 10-min interval (as in F12). While it is conventional for studies utilizing well-documented radar data assimilation procedures to focus solely on the forecast period for evaluation, this work also examines the assimilation period, because no studies have yet statistically evaluated an approach assimilating total lightning data over a large sample of forecast days. To examine how this approach works in a wide variety of conditions, these forecasts were conducted in real time at

[1] In F12, the labels of the curves in Fig. 7 associated with the graupel mass constants: "0.5 and 1 g kg^{-1}" should instead read "1 and 1.5 g kg^{-1}."

convection-allowing scales over a relatively large domain. Such an analysis is necessary to illustrate how this assimilation scheme spins up the convection and, thus, to shed light on how the forecast is affected.

3. Evaluation procedures

The first part of this study focuses on a general evaluation of the simulated bulk total and average APCP fields using various standard approaches with the exception of aggregate composite frequency diagrams, which are devised to identify potential systematic displacement errors in the simulated convection. The aggregate composite frequencies of forecast rainfall relative to observed rainfall were computed following the procedure outlined in Clark et al. [2010b; see Eq. (3)] within the mask area of the simulation domain (Fig. 2). The compositing procedure is implemented as follows: looping through all the points on the horizontal plane within the mask area (Fig. 2), the algorithm first determines a set of grid points G where the observed APCP is greater than or equal to a given threshold (ranging from 2.5 to 50 mm). For each of the grid points in G, a square of predetermined area of 640 km $\times$ 640 km centered at this point is then constructed. Each of the grid points within each square is then either assigned a hit (''1'') if the aforementioned APCP threshold was at least met in the simulation or assigned a miss (''0'') otherwise. This procedure was repeated for each of the 67 cases with all the hits summed yielding a 160 $\times$ 160 size array (i.e., 640 km $\times$ 640 km) with the grand totals of hits. These totals are then normalized by the number of grid points in the mask area in Fig. 2 and by the number of cases (Fig. 1). These calculations were performed for the APCP thresholds of 2.5, 5, and 10 mm over 1-, 3-, and 6-h accumulation intervals.

The second part of this work, which focuses on a statistical evaluation of the simulations, employs aggregated neighborhood-based equitable threat scores (ETSs) following Clark et al. [2010b; Eqs. (1) and (2)] as the chief metric to evaluate the overall skill of the lightning assimilation scheme described in section 2b. Defined this way, an ETS of 1.0 indicates a perfect forecast (ETS of 0.0 means no skill), and $-1/3$ is the lower limit.

To calculate the final ETS values, two main iterations were utilized. During the first iteration, contingency table elements were derived for each day and simply summed over all 67 cases (Fig. 1) to yield an (initial) aggregate ETS value. The aggregate and case-specific ETSs were computed for the APCP thresholds of 2.5, 5, and 10 mm over 1-, 3-, 6-, 12-, and 24-h accumulation intervals. Higher thresholds of 15, 25, and 50 mm were considered for the APCP at 6-, 12-, and 24-h accumulation intervals. For each of the aforementioned six APCP thresholds and five APCP periods, the following nine neighborhood radii around each scalar point [i.e., the geometrical center of the grid cell, see Fig. 5 of Clark et al. (2010b)] were considered: r = 0, 4, 8, 12, 16, 20, 24, 32, and 40 km. In this manuscript, the notation $\langle \mathrm{ETS} \rangle_r$ refers to the aggregate ETS value at a radius r, following the nomenclature employed in Clark et al. (2010b). Thus, $\langle \mathrm{ETS} \rangle_0$ is equivalent to the conventional gridpoint-based ETS. As noted in many studies (Casati et al. 2008; Roberts and Lean 2008; Ebert 2009; Schwartz et al. 2010; Clark et al. 2010b), neighborhood-based methods are advantageous because they reduce the occurrence of ''double penalty'' events associated with small displacement errors in the model. This is achieved by relaxing the requirements for hits, misses, and false alarms by also considering the adjacent grid points within the prescribed radius (Ebert 2009). Using the contingency data required to derive the $\langle \mathrm{ETS} \rangle_r$, the associated bias was computed simultaneously for each single day and in the aggregate. The bias was calculated because past studies have shown that high/low bias can significantly impact the ETS (Baldwin and Kain 2006; Clark et al. 2010b). Thus, if a high or low bias was obtained, a second iteration (below) was devised to account for it.

To compute the final ETS values, a second iteration was subsequently performed whereby a bias correction toward 1 (i.e., perfect forecast) was applied using the formerly computed contingency tables and biases for each of the 67 days. As noted in Hamill (1999), Mesinger (2008), and Clark et al. (2010b), a bias correction allows for a more even-handed comparison between given sets of model forecasts [e.g., quartiles of APCP distribution; Jenkner et al. (2008)] and a more reasonable estimation of position errors. The bias correction algorithm was applied iteratively on each case as follows: for each time interval where the bias exceeds (is smaller than) a nominal value of ~1.3 (~0.7), the 2D APCP data at that time were converted into a 1D array. The APCP values in this 1D array were then sorted in ascending order to facilitate the determination of the new APCP threshold, which are subsequently used to update the contingency data and ETS (hereafter BC-ETS). For a bias exceeding 1.3, the algorithm increases the APCP threshold to lower the bias, while for bias $<$ 0.7, the algorithm finds a sufficiently lower APCP threshold to increase the bias. For bias values between 0.7 and 1.3, no action was taken, because additional analysis revealed that the aggregate bias is primarily affected by bias values that generally lie outside the (0.7:1.3) range. Note that the initial null bias value was not altered in the algorithm because it is expected that no convection would be present initially in the model.

The differences between bias-corrected and uncorrected values of aggregate ETS in this study's forecasts were ≤0.05. Clark et al. (2010b) found that noticeable differences (i.e., ~0.1) between the bias-corrected and uncorrected aggregate ETS were more consistently seen when the following conditions were met: (i) the APCP threshold was >10 mm, (ii) the APCP intervals were ≥3 h, and (iii) the neighborhood radius was ≥8 km. In a test (not shown) of our forecasts using r = 40 km and an APCP threshold of 25 mm for 3-h APCP intervals, correcting the bias to ~1 improved the aggregate ETS by ~0.1.

To determine the statistical significance (at the 95% confidence) of the computed differences between the BC-ETS from LIGHT and CTRL, a bootstrap resampling technique (repeated 1000 times) was applied onto each set of bias-corrected contingency table elements following a methodology described in Hamill (1999) and used in Clark et al. (2010b).

To contrast the above BC-ETS results with another neighborhood-bases metric, the last part of this statistical analysis focuses on evaluating the skill of LIGHT using the fraction skill score (FSS) method as defined by Roberts and Lean (2008). FSS is a variant of the fraction Brier score (FBS; Roberts 2005) and is an attractive measure of skill on finescale grids primarily because, at a given neighborhood radius, small displacement errors are less penalized than with the ETS. FSS divides the original FBS by a hypothetical "worst-case FBS" which, akin to the original FBS, is a function of the observed and simulated fractions. FSS ranges from 0 (no skill) to 1 (perfect forecast). Perhaps the chief limitation of FSS lies in its inability to account for bias, which is elevated in the current simulations, especially for LIGHT (Fig. 7). This limitation is particularly relevant, given the relatively large sample size herein. Because of this drawback, the FSS was computed on the bias-corrected contingency data. The neighborhood area in the original method from Roberts and Lean (2008) consists of squares (their Fig. 2), while the Clark et al. (2010b) neighborhood approach employs disks (their Fig. 5). Although quantitative differences in FSS are expected to arise from using either definition of neighborhood areas, they are expected to remain negligible, especially on the aggregate.

4. Results

To provide a comprehensive view of the performance of the LIGHT runs, this section is divided into two parts. The first focuses on directly comparing the APCP values (summed and averaged across all 67 cases) between CTRL, LIGHT, and the stage-IV data (referred to as "OBS" in the remainder of the manuscript). The second part presents the statistical analysis described in section 3.

a. General evaluation

Before providing a statistical perspective of the performance of LIGHT, it is useful to illustrate qualitatively how the spatial distribution of APCP fields differ between LIGHT, CTRL, and OBS. The first intuitive step is to evaluate how various differences in total APCP (i.e., summed over all 67 cases) between the above three datasets are distributed over the area of interest (Fig. 2) and evolve over time. The difference in the 0–3-h APCP fields summed over all 67 cases between CTRL and OBS (Figs. 3a,b) and LIGHT and OBS (Figs. 3b,d), show a general tendency for LIGHT to significantly overestimate the 0–3-h APCP. In contrast, CTRL tends to underestimate the 0–3-h APCP (Fig. 3a) owing to a delay in convection initiation (CI) incurred by the initial model adjustment (or spinup; Skamarock 2004; Kain et al. 2010a). Considering the 0–24-h APCP fields, the same general qualitative behavior for LIGHT and CTRL is seen for the Great Plains (cf. Figs. 3b,d). A noticeable positive difference in the precipitation fields is also noted over the East Coast and the Southeast United States for both LIGHT and CTRL. This indicates that the model tends to overpredict late afternoon airmass convection, which may arise partly from errors in the initial and boundary conditions. The fields in Fig. 3 contain a great deal of small-scale variability, probably due to the relatively small sample size that allows individual events to exert considerable influence, particularly MCSs in the Great Plains (Fig. 3c).

Hovmöller diagrams of latitudinally averaged APCP over the eastern two-thirds of the United States (i.e., within the mask area of Fig. 2) corroborate the aforementioned behavior: As shown in Fig. 4e, during the first 6 h of the simulations, LIGHT (Fig. 4c) clearly overestimates the stage-IV APCP (OBS Fig. 4a), especially within the longitudinal belt geographically consistent with the Great Plains (99°–87°W). Although of lesser magnitude, CTRL (Fig. 4b) also overestimates the APCP between 3 and 6 h, while largely underestimating APCP during the first 3 h of simulation (Fig. 4d) owing to the initial model spinup (Skamarock 2004; Kain et al. 2010a). As shown in Figs. 3b and 3d, the overestimation of the LIGHT-generated APCP is carried over to the 0–24-h APCP. Figures 4d–f also illustrate that the largest differences seen between CTRL and LIGHT occur during simulation hours 1–6 (i.e., during and shortly after the 2-h assimilation period). After 12 h of simulation the difference in solutions becomes increasingly smaller.

To better illustrate the integrated impact of the assimilation of lightning data on the simulated APCP, the total water substance mass (APCP mass + total hydrometeor and water vapor mass) and total APCP mass

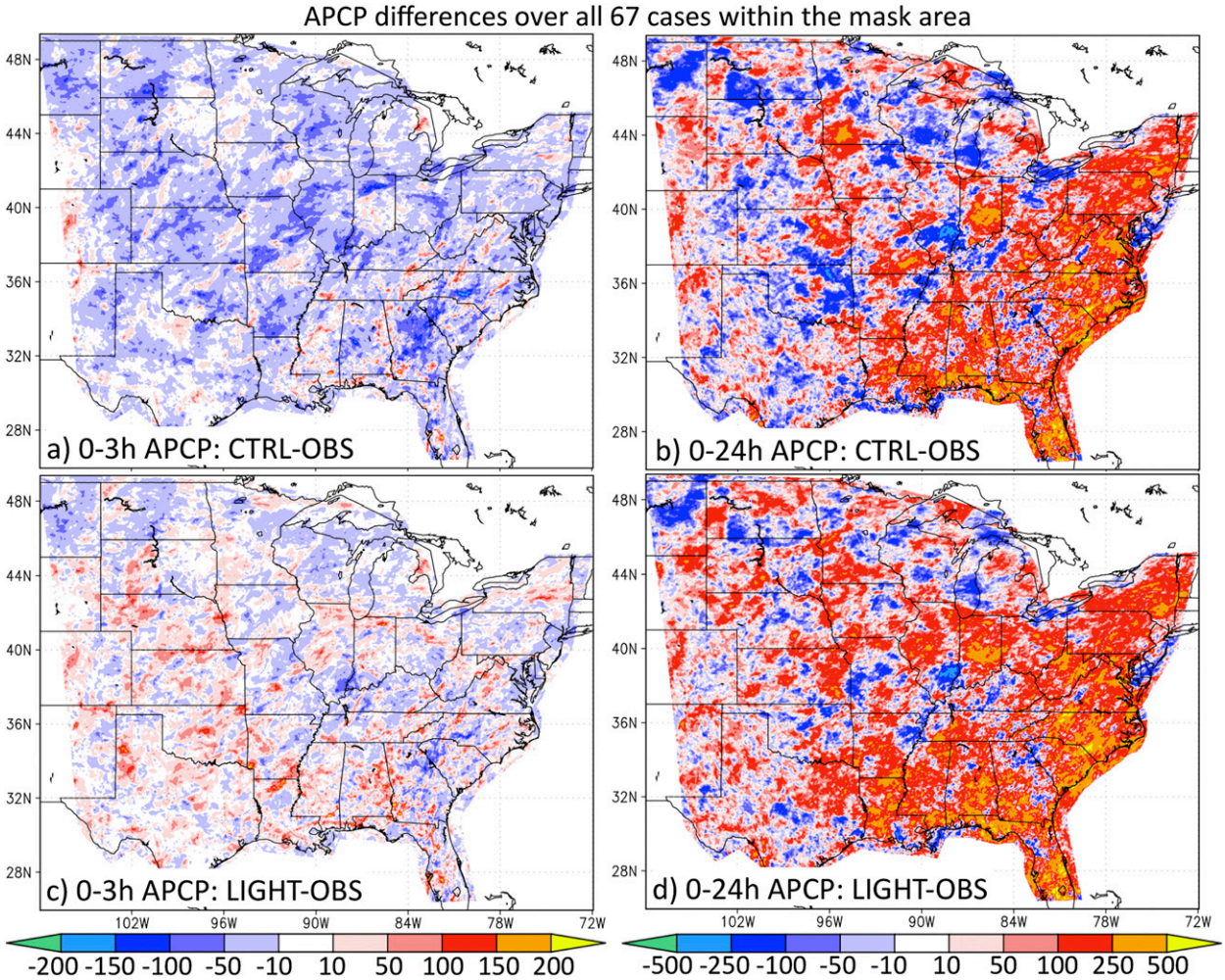

FIG. 3. Difference of the total 0–3- and 0–24-h accumulated precipitation (APCP, mm) over all the 67 cases (Fig. 1) and the stage-IV data (OBS) within the mask area shown Fig. 2. (a) Total 0–3-h APCP differences between CTRL and OBS. (b) As in (a), but for the 0–24-h APCP. (c),(d) As in (a),(b), but for the APCP differences between LIGHT and OBS.

averaged over all 67 cases were computed at the first hour of simulation (i.e., 0100 UTC). Recalling that the model output was saved every hour and that the lightning assimilation was conducted during the first two hours of simulation (i.e., 0000 until 0200 UTC), 0100 UTC was selected because the unconstrained model (i.e., CTRL) is still in the process of spinning up the convection, as evidenced by the overall lack of APCP at this time in CTRL (Fig. 4b) compared to LIGHT (Fig. 4c). Averaged over all days, the lightning assimilation scheme increases the total water substance mass by about 0.5%. Both the total hydrometeor and APCP masses are roughly doubled and equal to about 85% of the added water vapor. It is unknown how much of the added vapor is directly converted to hydrometeors. Much of the added vapor may remain as vapor and be exhausted by anvil-level detrainment, while induced updrafts may draw up environmental moisture that actually results in much of the hydrometeor mass. In both CTRL and LIGHT, the total hydrometeor mass is about two orders of magnitude larger than the accumulated precipitation at 1 h, suggesting that many storms have not reached maturity (e.g., towering cumulus stage) and not yet precipitating efficiently. These same calculations were also performed for the 29 June 2012 derecho case of F14 and revealed remarkably consistent results. It was also found that the fraction of water substance mass added by the lightning assimilation (0.6%) is about one order of magnitude smaller than the fraction added by the cloud analysis (9%) of the three-dimensional variational data assimilation system of Gao et al. (2013), which was also tested in F14.

A closer inspection of hourly radar reflectivity composite plots for each of the 67 cases helped to elucidate the chief reasons for the tendency of LIGHT to overestimate APCP in the Great Plains during the first 6 h of

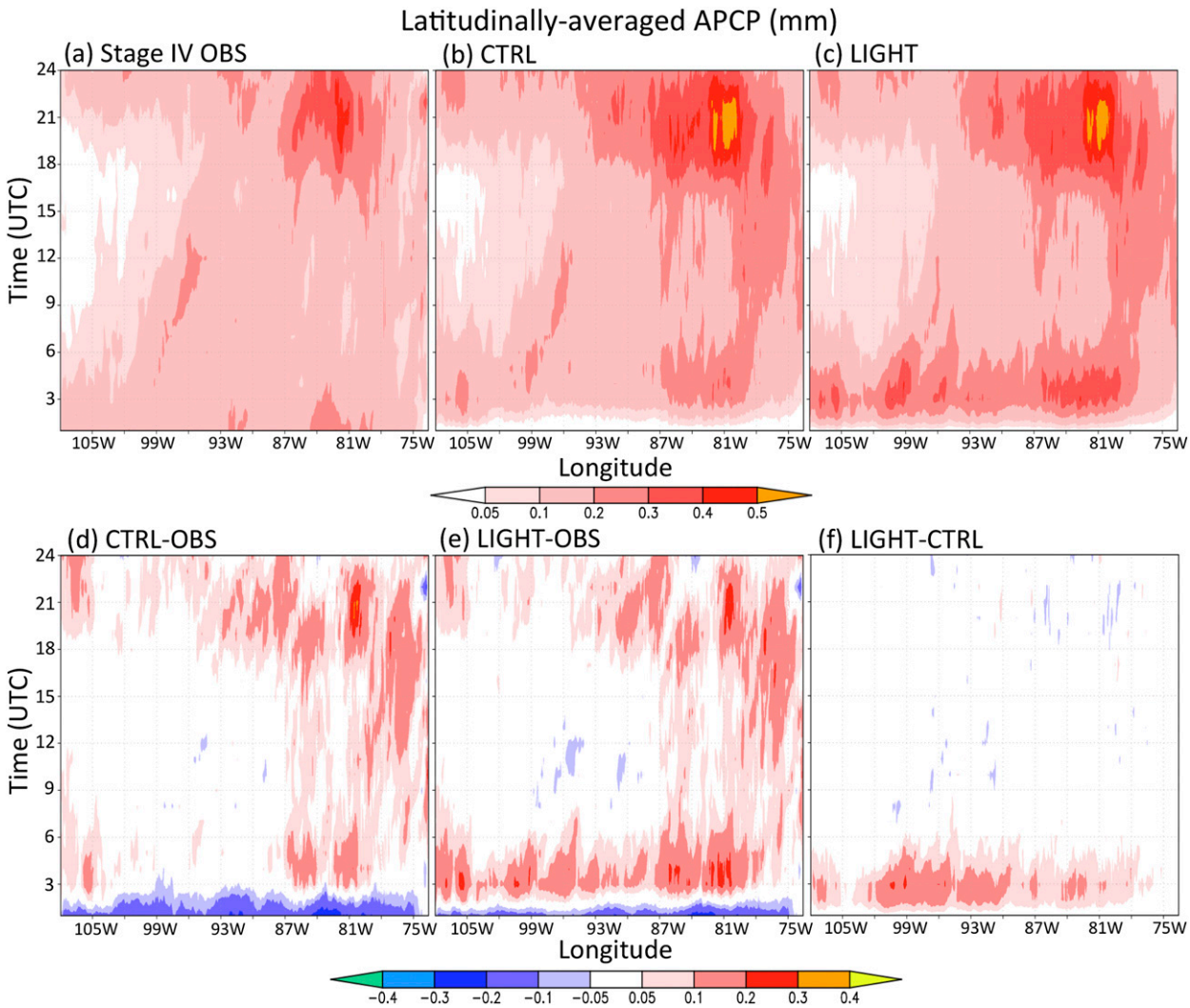

FIG. 4. Hovmöller diagrams of latitudinally averaged APCP (mm) over all 67 cases along the longitudinal belt delineated by the mask in Fig. 2 for (a) stage-IV rainfall estimates (OBS), (b) CTRL, and (c) LIGHT. (d)–(f) Differences between the latitudinally averaged APCP (over all 67 cases) of CTRL and OBS, between LIGHT and OBS and between LIGHT and CTRL, respectively. Legends for colors and shading are shown at the bottom of each corresponding row.

simulations. Nocturnal MCS commonly occur in the Great Plains in the May–July time period (e.g., Maddox 1980) and typically develop or begin to mature near the time when the present simulations were initialized (i.e., 0000 UTC). In fact, of the 67 days considered herein, about 18 (~27%) had an MCS or squall line during the first 6 h of simulation. Because these MCSs are copious lightning (and rainfall) producers (Goodman and MacGorman 1986; F14) and generally are driven by large-scale features that are reasonably well captured by the 40-km NAM-derived initial conditions (e.g., low-level jet, fronts, and axes of instability), the LIGHT runs reasonably reproduce their overall evolution (Fritsch et al. 1986) by quickly generating convection and associated mesoscale cold pools near the correct locations. Owing to the relatively large area of the lightning density fields associated with MCSs, however, the lightning assimilation scheme will add water vapor over a large area (and volume), which would further exacerbate any preexisting positive APCP bias. This is because some of this added moisture will, through microphysical processes, eventually be converted to surface precipitation. The severity of the bias incurred by the assimilation, however, could partially be curtailed by (i) reducing the volume where nudging is applied (decreasing coefficient A or assimilate over a shallower layer) and/or (ii) using a shorter assimilation time window and/or (iii) reduce the absolute amount of water vapor mass added per time step by the scheme (through coefficients B, C, and/or D). For instance,

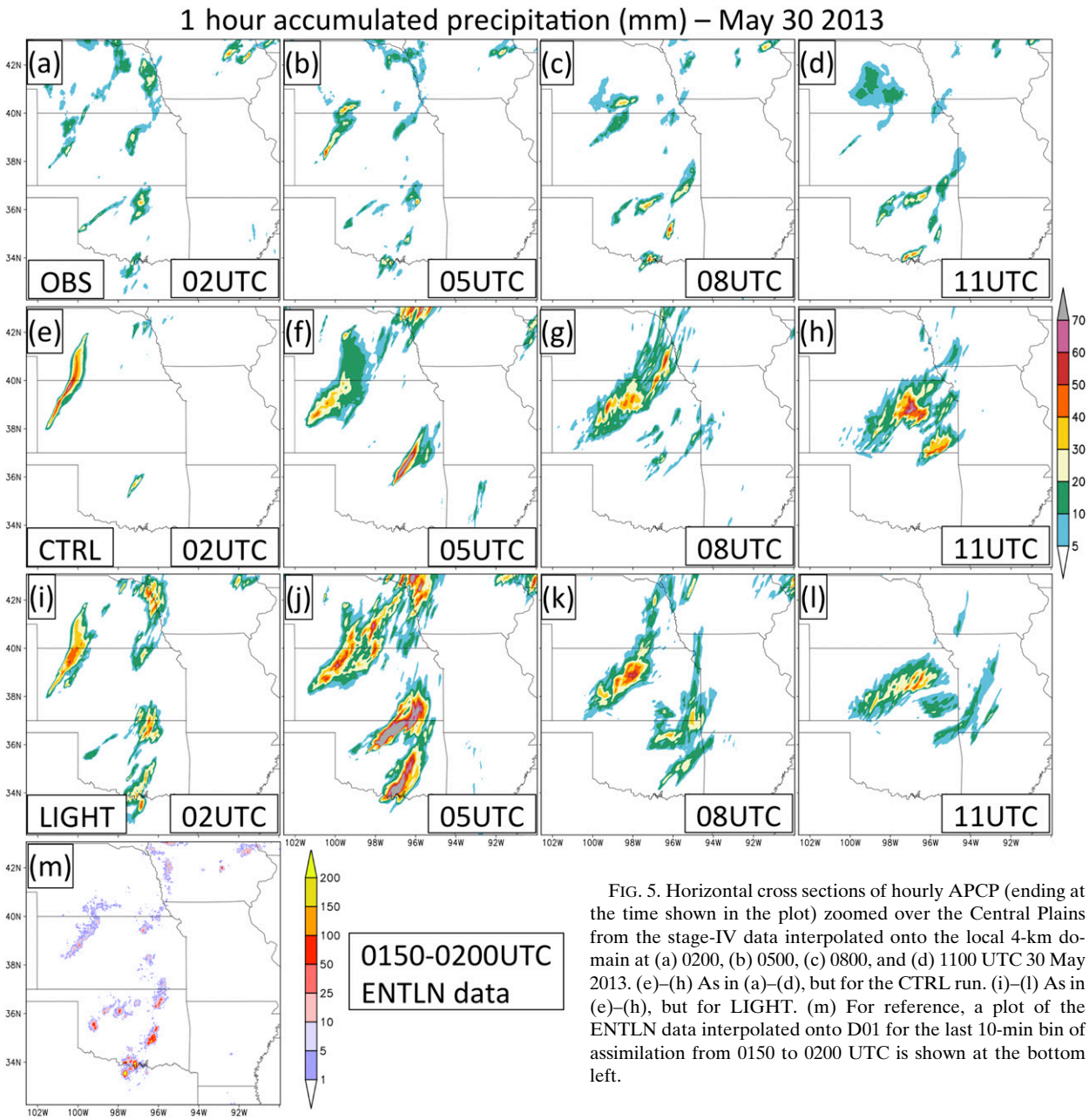

FIG. 5. Horizontal cross sections of hourly APCP (ending at the time shown in the plot) zoomed over the Central Plains from the stage-IV data interpolated onto the local 4-km domain at (a) 0200, (b) 0500, (c) 0800, and (d) 1100 UTC 30 May 2013. (e)–(h) As in (a)–(d), but for the CTRL run. (i)–(l) As in (e)–(h), but for LIGHT. (m) For reference, a plot of the ENTLN data interpolated onto D01 for the last 10-min bin of assimilation from 0150 to 0200 UTC is shown at the bottom left.

reducing B from the current high value of 0.2 to 0.05 (i.e., limit the maximum nudging to water saturation) yields smaller areal coverage of simulated 1-h APCP contours $\geq\sim$20 mm (not shown).

To illustrate the ability of the lightning assimilation to beneficially force the evolution of nocturnal convection and MCSs and, simultaneously, to amplify an already existing positive APCP bias in CTRL, a representative example of the evolution of the APCP fields for the 30 May 2013 multi-MCS case over the Nebraska–Kansas–Oklahoma area is provided in Fig. 5. The geographical area in Fig. 5 contains most of the lightning that was detected by the ENTLN during the first 2 h of simulation. The difference in BC-ETS values for this particular case was also higher than the aggregate at all thresholds by as much as 0.1, highlighting the tendency for this lightning assimilation scheme to perform particularly well during MCS days. A side-by-side comparison between the last 10-min bin (0150–0200 UTC) of the assimilated ENTLN data and the LIGHT APCP fields at 0200 UTC revealed a high spatial agreement (Figs. 5m and 5i) in contrast to CTRL (Figs. 5m and 5e). There are

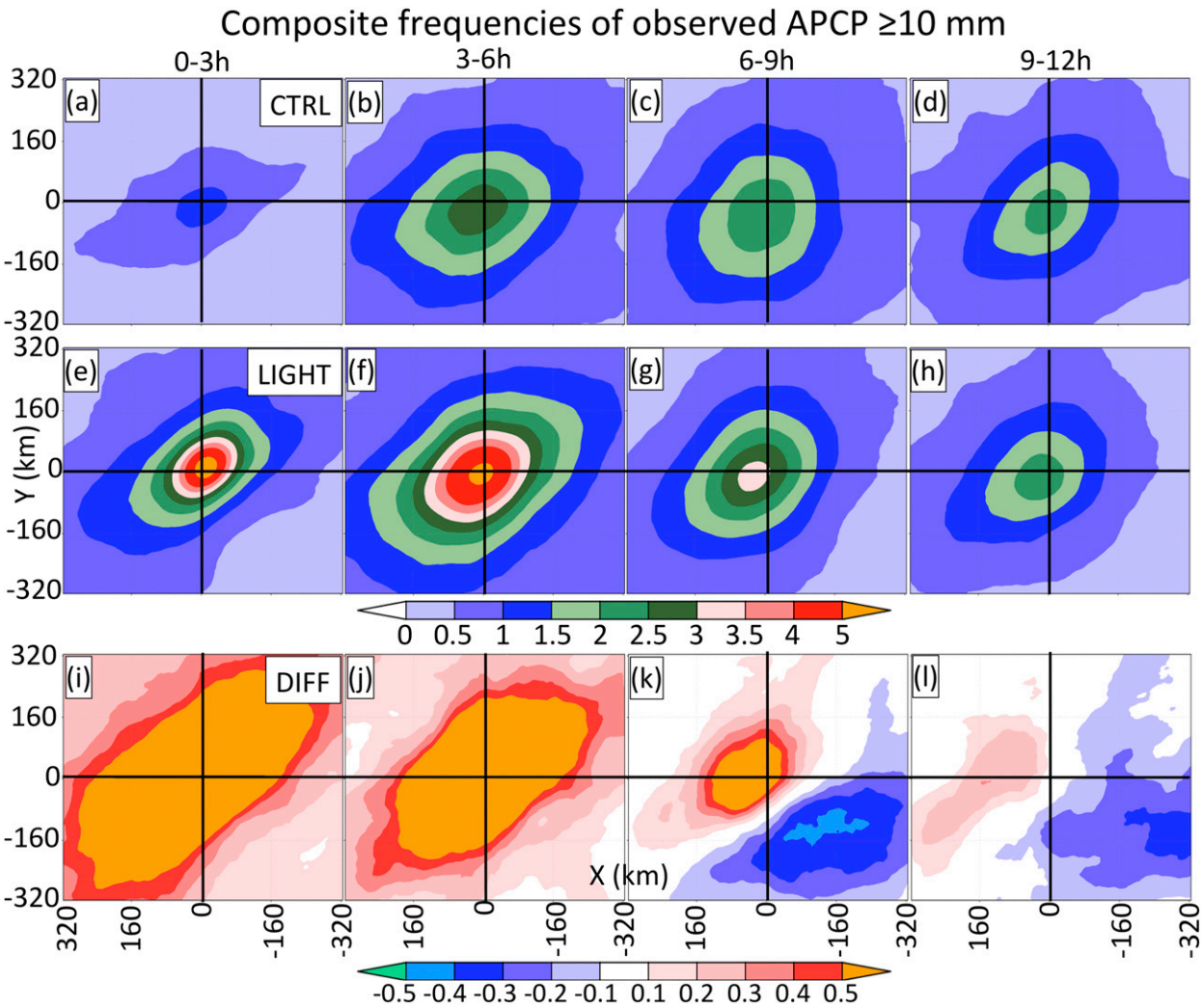

FIG. 6. (a)–(d) Composite frequencies of grid points forecasting 3-hourly APCP ≥ 10 mm relative to the observed 3-hourly APCP ≥ 10 mm for the CTRL run during each 3-h intervals contained during the first 12-h simulation. (e)–(h) As in (a)–(d), but for LIGHT. (i)–(l) Differences of the composite frequencies between LIGHT and CTRL. The composite frequencies were normalized by the number of grid points in the mask area shown in Fig. 2 and by the number of cases in Fig. 1. Legends for color and shadings are shown at the bottom of the corresponding row(s) with the numbers shown under each color bar scaled (multiplied) by a factor of 1000.

still areas of observed lightning, however, without any discernable APCP collocated with it (e.g., 35°N, 96°W in Figs. 5m and 5i), which arise for two main reasons: (i) the time scale (delay) necessary to generate light-to-moderate precipitation at the surface (defined here as rates of 5 mm h^{-1}) after initiation of convective overturning via the assimilation is on the order of 10–15 min; and (ii) errors in the local environment advanced from imperfect large-scale fields in the initial conditions may further exacerbate this delay or, for low flash rate storms, suppress the convection forced by the assimilation. Although less evident, a similarly noteworthy spatial collocation is seen between the ENTLN fields and OBS at 0200 UTC (cf. Figs. 5m and 5a). Despite this good spatial agreement between LIGHT and OBS, the LIGHT APCP fields clearly are overestimated by almost an order of magnitude in some places (e.g., convection of Oklahoma, Figs. 5b and 5j). Note that CTRL also exhibits a tendency to overestimate APCP after the end of the spinup period at about 0200 UTC (e.g., Figs. 5b and 5f). During the spinup period, however, the CTRL-simulated APCP generally are smaller than observed (<20 mm, not shown), consistent with the results shown earlier (Figs. 3 and 4). As will be shown in the subsequent section, this systematic overestimation in APCP accounts for an initially high (>1.5) aggregate bias after 0200 UTC for both CTRL and LIGHT. In summary, CTRL and LIGHT each have good and bad features depending on the forecast hour with LIGHT performing generally best at the analysis time (0200 UTC) and CTRL showing

overall a reduced positive APCP bias relative to LIGHT throughout the forecast.

Later in the day during the afternoon hours (1800–0000 UTC), which corresponds to the last 6 h of the simulations herein, diurnal airmass thunderstorms are common, particularly over the eastern and southeastern United States. Owing to their comparatively much smaller (i) characteristic length scale (e.g., Bryan et al. 2003), (ii) ''cell-scale'' lightning footprint, and (iii) flash rates, and because the lightning assimilation ceased more than 16 h before this time period, both CTRL and LIGHT produce similar radar reflectivity fields (not shown). As will be shown in the next section, the difference in skill between LIGHT and CTRL tends to become statistically insignificant ($\alpha = 0.05$) past 9–12 h of the simulations as the overall solution tends to become bounded by the NAM-derived large-scale environment. One potential factor for this behavior may arise from the solution becoming progressively more saturated with error on the convective scale at later times. A hint of this behavior can be seen in Fig. 5 when comparing the simulated APCP fields between LIGHT and CTRL at 0500 and 1100 UTC (Figs. 5f,h,j,l); initially the differences in simulated APCP between LIGHT and CTRL are larger, in contrast to later on in the simulation. Other studies also found that the improvements incurred by the assimilation of lightning (e.g., Mansell et al. 2007) or radar data (e.g., Hu et al. 2006; Sugimoto et al. 2009; Jones et al. 2014) wanes generally after about the first 6 h of forecasts.

To identify potential systematic displacement errors and generalize the above findings further, aggregate composite frequencies of forecast rainfall relative to observed rainfall within the mask area of the simulation domain (Fig. 2) are shown in Fig. 6. The composite frequencies of forecast rainfall above a 3-hourly APCP threshold of 10 mm for LIGHT and CTRL (Fig. 6) further corroborates some of the findings drawn from Figs. 3–5. During the first 6 h of simulation, LIGHT exhibits the highest frequencies, which are much larger than those of CTRL (cf. Figs. 6a,b and 6e,f), particularly during the first 3 h of simulation, as illustrated by the large differences seen between the two (Figs. 6i,j). Notably, these relatively higher frequencies are consistent with the large positive bias in the simulated APCP for LIGHT (Figs. 3 and 4). Overall, no significant horizontal displacement of the maximum frequency contours of the simulated APCP relative to the OBS is noted for either CTRL or LIGHT (Figs. 6a–h). During the subsequent simulation time window (6–9 h), the difference in composite frequencies reveals that LIGHT still exhibits better skill than CTRL as indicated by large positive differences near the center (zero displacement) of the

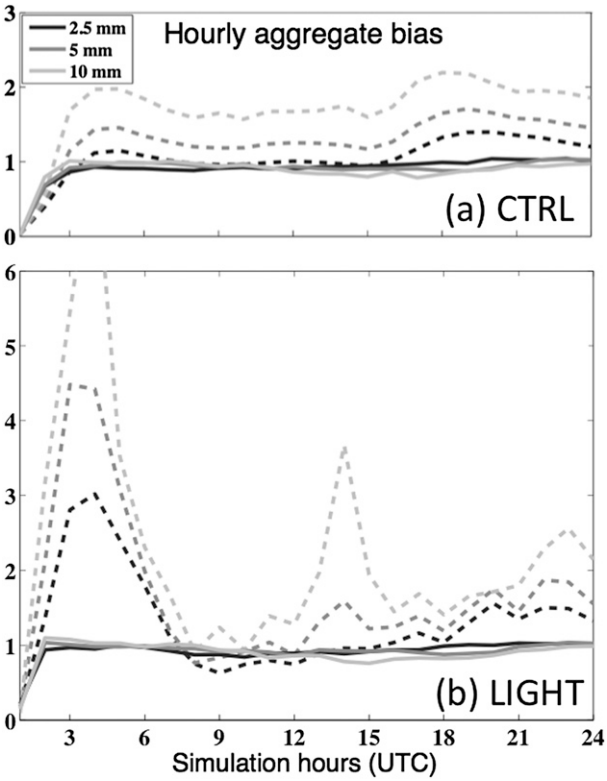

FIG. 7. Aggregate bias for hourly APCP of 2.5, 5, and 10 mm before (dashed) and after (solid) the correction was applied for (a) CTRL and (b) LIGHT. Legends are shown in the top-left corner of (a).

plot (Figs. 6c,g,k). Later in the simulation, (9–12 h, Fig. 6k, 12–24 h, not shown), LIGHT shows higher APCP frequencies to the west (and lower values to the east) relative to CTRL. This relative spatial displacement error for LIGHT is consistent with a general tendency for WRF forecasts on either convection-allowing or -parameterizing grids to exhibit a westward position bias (Grams et al. 2006; Clark et al. 2010b), which could partly arise from problems in accurately depicting the zonal movement of MCSs. Similar westward position errors were found with the NAM on convection-parameterizing grids (Wang et al. 2009). The greater composite frequencies also indicate a southwest–northeast alignment during the first 6 h of simulation, particularly for LIGHT (cf. Figs. 6a,b and 6e,f). This particular orientation likely arises from the convection being preferentially forced along fronts, whose typical orientation over CONUS during this time of year lies generally in a southwest–northeast direction. In line with the previous results drawn from Figs. 3–5, the comparatively small differences in frequencies after 15 h of simulation (not shown) offers an alternative view of the previously documented behavior whereby the model solution of LIGHT progressively converges to that of CTRL as the former

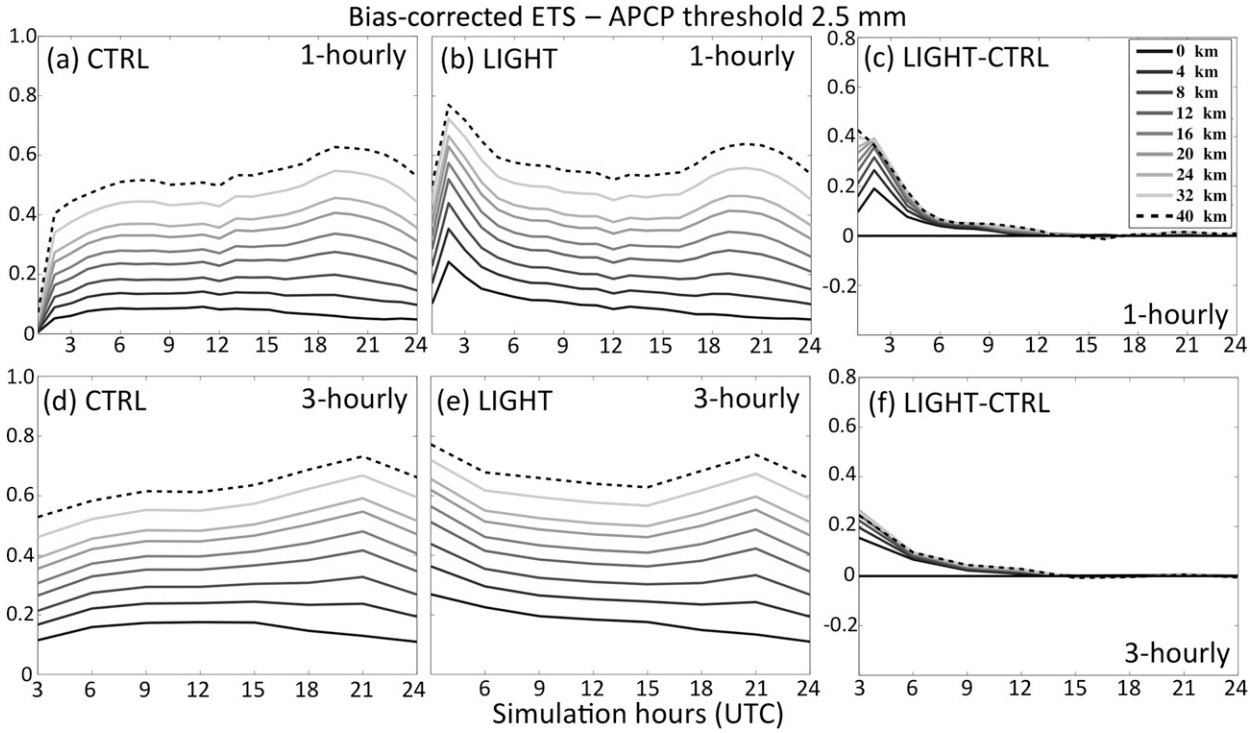

FIG. 8. Aggregate BC-ETS for the 1-h APCP threshold of 2.5 mm for (a) CTRL, (b) LIGHT, and (c) the difference between LIGHT and CTRL. (d)–(f) As in (a)–(c), but for 3-hourly APCP. BC-ETS are shown for all the nine neighborhood radii considered in this study, with the legend shown in (c).

becomes bounded by the environmental conditions provided by the initial and boundary conditions derived from the NAM dataset.

b. *Statistical analysis*

As mentioned earlier, ETS were subject to two iterations wherein the initial bias estimates were utilized in the subsequent bias-correction step to yield a bias-corrected ETS (or BC-ETS). Figure 7 illustrates for the 1-h APCP how the algorithm corrects the initially high (aggregated) bias for both CTRL and LIGHT toward a general nominal value near 1 (perfect forecast). Figure 7b also shows that initially, the bias for LIGHT is much larger during the first 6 h of forecast—with peak values exceeding 6.0 at simulation hours 5 and 6. This is consistent with the previously documented tendency for LIGHT to significantly overestimate the APCP relative to CTRL during this time period (cf. Figs. 3, 4, and 5). During the first 3 h of simulation, however, CTRL is still in the process of spinning up convection, which explains the generally low initial bias seen at simulation hours 1 and 2 (Fig. 7a). This initial low bias is consistent with the generally negative total differences in 0–3-h APCP seen between CTRL and OBS throughout the analysis domain (Figs. 2 and 3a).

Looking at the BC-ETS statistics in Fig. 8, the hourly APCP for a threshold of 2.5 mm is significantly improved during the first 5 h of simulation (i.e., 3 h after the lightning assimilation ceased) for all nine neighborhood radii considered herein (Figs. 8a–c). Consistent with the results presented earlier in Figs. 3 and 4, the BC-ETS differences between LIGHT and CTRL progressively converge toward the same value (Fig. 8c). A similar behavior is concordantly seen for the 3-hourly APCP (Figs. 8d–f) with generally slightly higher BC-ETS for both CTRL and LIGHT because of an increasing chance of reaching a given APCP threshold over a 3-h period relative to a 1-h period (i.e., more hits).

Results for 1-, 3-, and 6-hourly APCP at a higher threshold of 10 mm are similar (Fig. 9) to the lower thresholds. Tables 1 and 2 further corroborate the improvements of the simulated APCP in the LIGHT runs for 12- and 24-h APCP at the thresholds of 10, 25, and 50 mm. When comparing both tables side by side it is easily noticed that the larger 0–24-h APCP BC-ETS for LIGHT is explained almost exclusively from the improvements of the 0–12-h APCP (as seen in Figs. 7 and 8). Given that the largest improvements in BC-ETS are seen during the first ~6 h of simulation, it is relevant to determine how much of the increased BC-ETS of the 0–24-h APCP in LIGHT is actually explained by the 0–2-h spinup (assimilation) period. Given an APCP threshold,

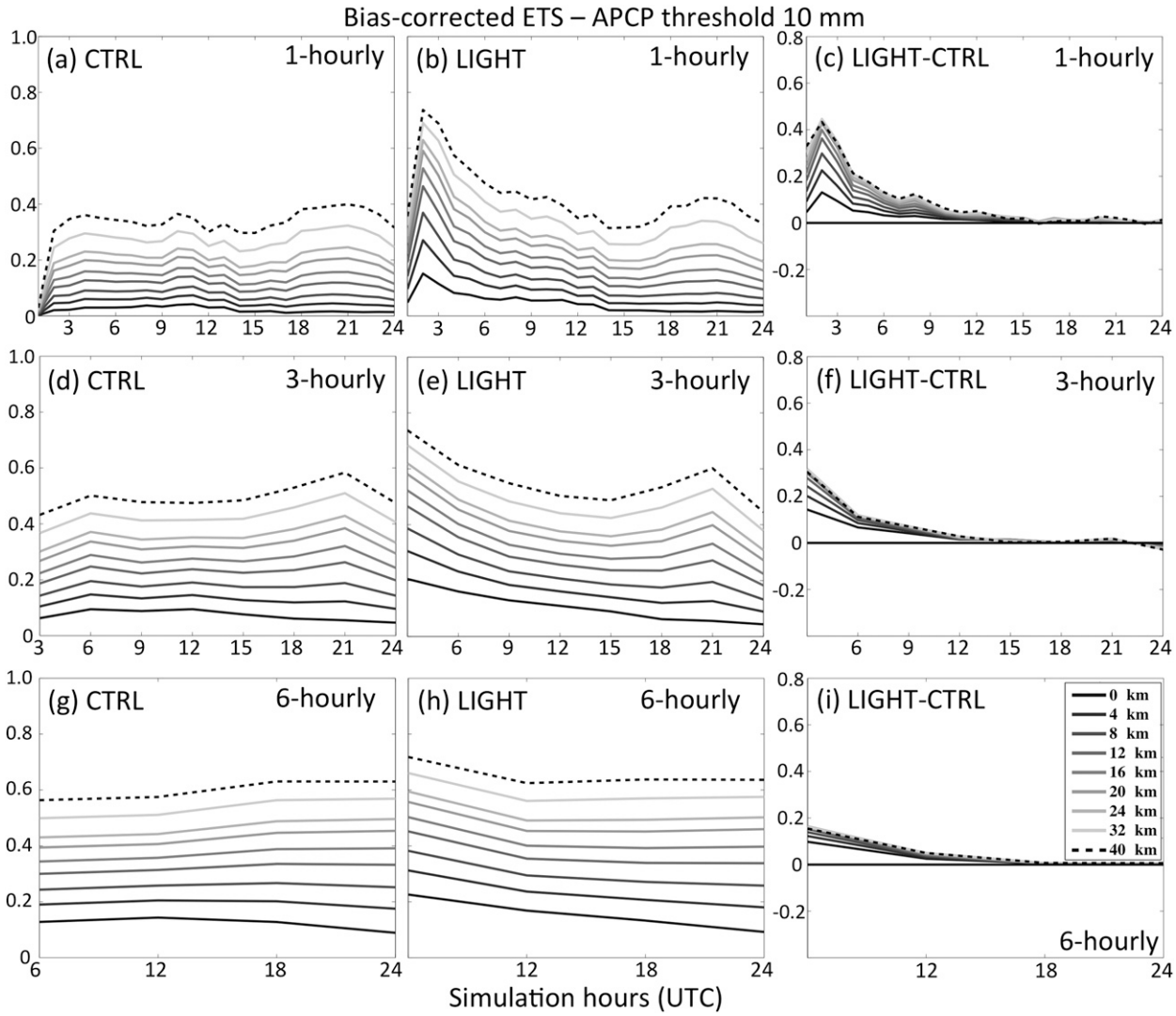

FIG. 9. (a)–(f) As in Fig. 8, but for an APCP threshold of 10 mm. Because of the higher threshold, (g)–(i) additionally shows the BC-ETS for 6-hourly APCP. Legends for all nine neighborhood radii are shown in (i).

the differences in BC-ETS for hourly APCP between LIGHT and CTRL first are computed for each nine radii. Then, the area under each of the curves of the BC-ETS differences is determined using the trapezoidal rule. The contribution of BC-ETS improvement from the spinup is then simply given by the ratio of the area under the curve between 0 and 2 h and the area under the curve between 0 and 24 h. At 10 mm, the contribution ranges from ~21.1% at $r = 0$ to ~26.5% at $r = 40$ km. The contribution from the spinup increases with increasing (hourly) APCP thresholds. For instance, the contribution of the spinup is reduced to ~16.4% at $r = 0$

TABLE 1. Bias-corrected aggregate equitable threat scores (BC-ETSs) over all 67 CTRL cases for selected neighborhood radii of 0 (i.e., gridpoint based), 4, 16, and 32 km (shown in the second row) for APCP thresholds of 10, 25, and 50 mm (shown in the top row). (from top to bottom) The BC-ETS are shown for the 0–12-, 12–24-, and 0–24-h APCP.

CTRL	10 mm				25 mm				50 mm			
Radius (km)	0	4	16	32	1	4	16	32	1	4	16	32
0–12 h	0.19	0.27	0.44	0.61	0.12	0.18	0.34	0.51	0.06	0.10	0.21	0.33
12–24 h	0.15	0.26	0.49	0.66	0.07	0.12	0.26	0.41	0.01	0.03	0.07	0.13
0–24 h	0.22	0.33	0.57	0.73	0.13	0.21	0.40	0.58	0.06	0.09	0.19	0.30

TABLE 2. As in Table 1, but for LIGHT.

LIGHT	10 mm				25 mm				50 mm			
Radius (km)	0	4	16	32	1	4	16	32	1	4	16	32
0–12 h	0.25	0.33	0.52	0.69	0.17	0.25	0.44	0.61	0.10	0.16	0.33	0.48
12–24 h	0.15	0.26	0.50	0.67	0.07	0.12	0.27	0.43	0.01	0.03	0.07	0.12
0–24 h	0.25	0.36	0.60	0.76	0.16	0.24	0.44	0.62	0.08	0.12	0.23	0.36

and to ~18.3% at $r = 40$ km at the APCP threshold of 2.5 mm.

To determine the statistical significance at the 95% confidence interval of the differences between the BC-ETS from LIGHT and CTRL, a bootstrap resampling test statistic (Hamill 1999) was conducted on those bias-corrected differences with key results shown in Fig. 10. Although the bias correction had overall little impact on the aggregate ETS values, the resampling was conducted on the bias-corrected differences for consistency with Figs. 8 and 9. The results were almost the same (BC-ETS differences between LIGHT and CTRL <0.05) when the resampling was applied to the uncorrected differences. For the 1- and 3-h APCP, the analysis revealed that, overall, the differences in BC-ETS remained insignificant past ~9 h of simulation (Figs. 10a–d). For the 6-h APCP, these differences became insignificant later after about 12 h of simulation (Fig. 10e). Results for 12-h APCP (at the higher thresholds of 10, 25, and 50 mm) showed that the BC-ETS differences remained significant for the 0–12-h APCP and insignificant for the 12–24-h APCP (not shown). Last, the difference in BC-ETS for the 24-h APCP in Tables 1 and 2 was marginally insignificant (not shown).

The ETS formulation can be viewed as a convolution between the probability of detection (POD), which accounts for the hits and misses and the false alarm rate (FAR), which accounts for correct rejections and false alarms. Thus, it is useful to determine the relative contributions of POD and FAR to the statistically significant BC-ETS improvements documented earlier (Figs. 9–10 and Tables 1 and 2). An example of FAR and POD evolution is shown in Fig. 11 for 1-h APCP at the 2.5- and 10-mm thresholds. As can be easily noted, the improvements in BC-ETS documented earlier during the first 12 h of simulation (e.g., Fig. 10), is attributed to a higher POD combined with a lower FAR in LIGHT relative to CTRL. An explanation for the higher BC-ETS values at higher neighborhood radii is that the POD increases and FAR decreases as the neighborhood radius increases (Fig. 11). Also, the tendency for BC-ETS differences between LIGHT and CTRL to increase with APCP thresholds at a given APCP interval (cf. Figs. 10a and 10b or Figs. 10c and 10d), can be explained by the evolutions of the respective differences of the FAR and POD between LIGHT and CTRL. For instance, for the 1-h APCP shown in Fig. 11, the positive difference (improvement) in POD increases as the APCP threshold increases (e.g., Figs. 11a,c), while, conversely, the difference in FAR between LIGHT and CTRL is seen to decrease as the APCP threshold increases (e.g., Figs. 11b,d). Concomitantly, the individual POD and FAR for LIGHT and CTRL decrease with increasing APCP threshold. This is because models have greater difficulty in forecasting the time and location of areas of high rainfall rates, especially those arising from smaller-scale convective features. In line with the BC-ETS results presented earlier, both the FAR and POD progressively converge to that of CTRL after 12 h of simulation with their differences (i.e., LIGHT − CTRL) becoming statistically insignificant after that. The same analysis conducted on 3-, 6-, and 12-h APCP yielded similar results (not shown).

Figure 11 also shows why the BC-ETS improved in LIGHT despite its noticeably larger aggregate bias. The much higher POD and slightly lower FAR in LIGHT indicates that, despite a tendency to overpredict precipitation, the method consistently succeeds in forcing some convection to be produced in the correct area, thereby yielding significantly more hits than in CTRL (see also Figs. 6e,f) while producing false alarm rates relatively similar (slightly lower) to those of CTRL. The slightly lower FAR in LIGHT arises from the development of spurious convection in the vicinity of the observed lightning locations being weakened or even suppressed by the compensating subsidence that is induced at the periphery of the forced convection (Fritsch and Chappell 1981).

To conclude this analysis, the remainder of this section will focus on FSS. For the sake of comparison and conciseness, the analysis will present results for 1- and 3-h APCP and focus on the first 9 h of simulation since BC-ETS differences were shown to be insignificant past this time for the 1- and 3-h APCP.

The aggregate FSS for 1- and 3-h APCP at the 2.5- and 10-mm thresholds are displayed in Fig. 12 and, overall, confirm the general results drawn earlier from the aggregate BC-ETS (Figs. 8 and 9). Notably, the most noteworthy improvements are seen at 2–4 h in the simulation with FSS differences (i.e., LIGHT − CTRL)

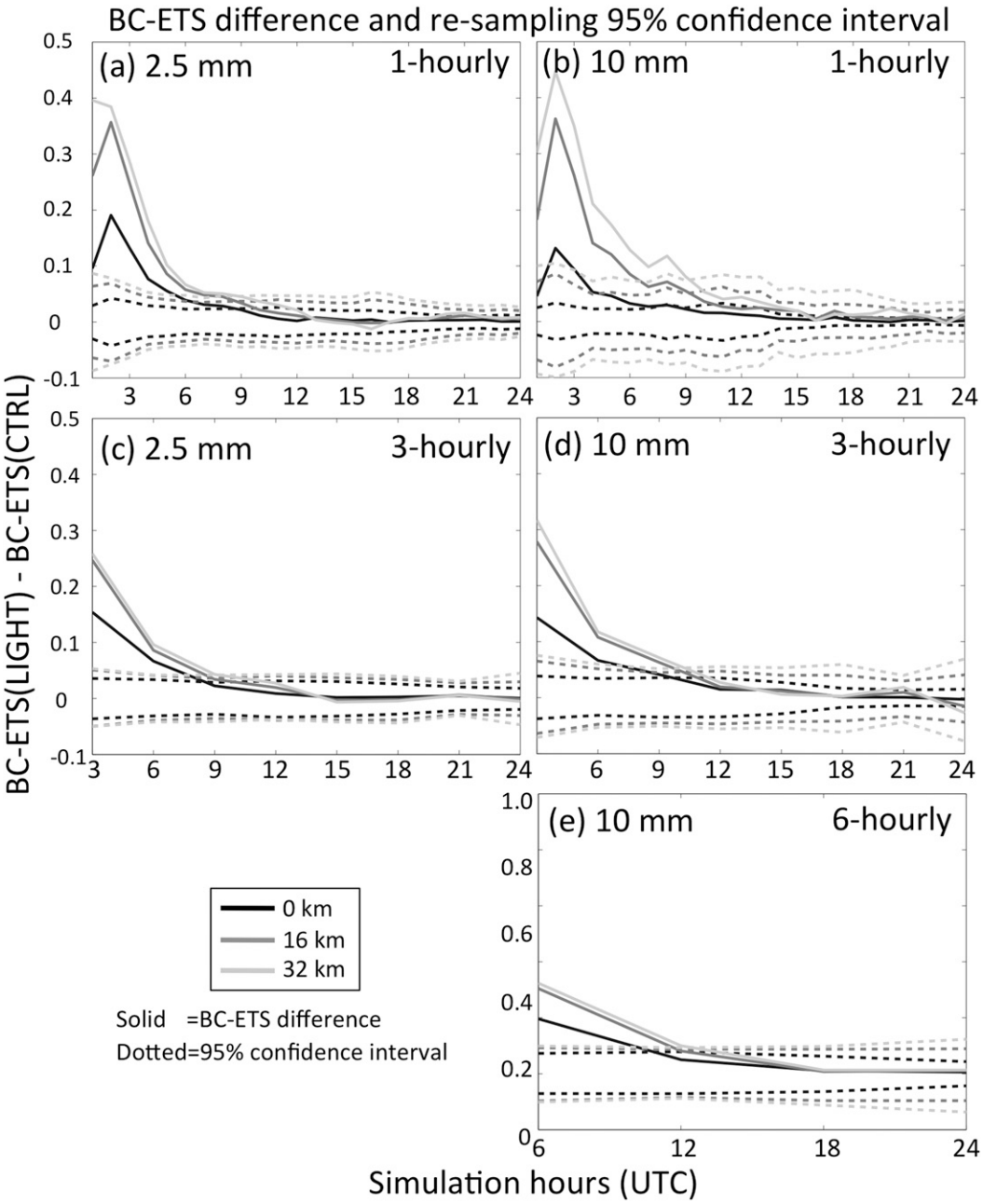

FIG. 10. BC-ETS difference (solid line) for the neighborhood radii of 0 km (gridpoint based), 16-, and 32-km overlaid with the 95% confidence interval (dotted line) of the BC-ETS difference computed using a 1000-sample bootstrap resampling of the contingency elements of all 67 cases for: (a) 1-h APCP with 2.5-mm threshold; (b) as in (a), but for a 10-mm threshold; (c) as in (a), but for 3-h APCP; (d) as in (b), but for 3-h APCP; and, finally, (e) as in (d), but for 6-h APCP. Legends for the curves are shown in the bottom-left corner of the figure.

reaching a maximum of 0.3 (Figs. 12f,i,l) or even 0.4 for 1-h APCP and 2.5-mm threshold (Fig. 12c). Similar to the BC-ETS, this positive difference progressively decreases toward small statistically insignificant values ($<|0.1|$, not shown) past 9 h of simulation. Results not shown for FSS for 6-, 12-, and 24-h APCP also remain consistent with those of the BC-ETS.

5. Summary

Using the WRF-ARW Model, a recently developed simplistic and computationally efficient lightning nudging scheme has been evaluated over 67 days spanning the 2013 North American warm season from May to July. The simulations were conducted in real time during

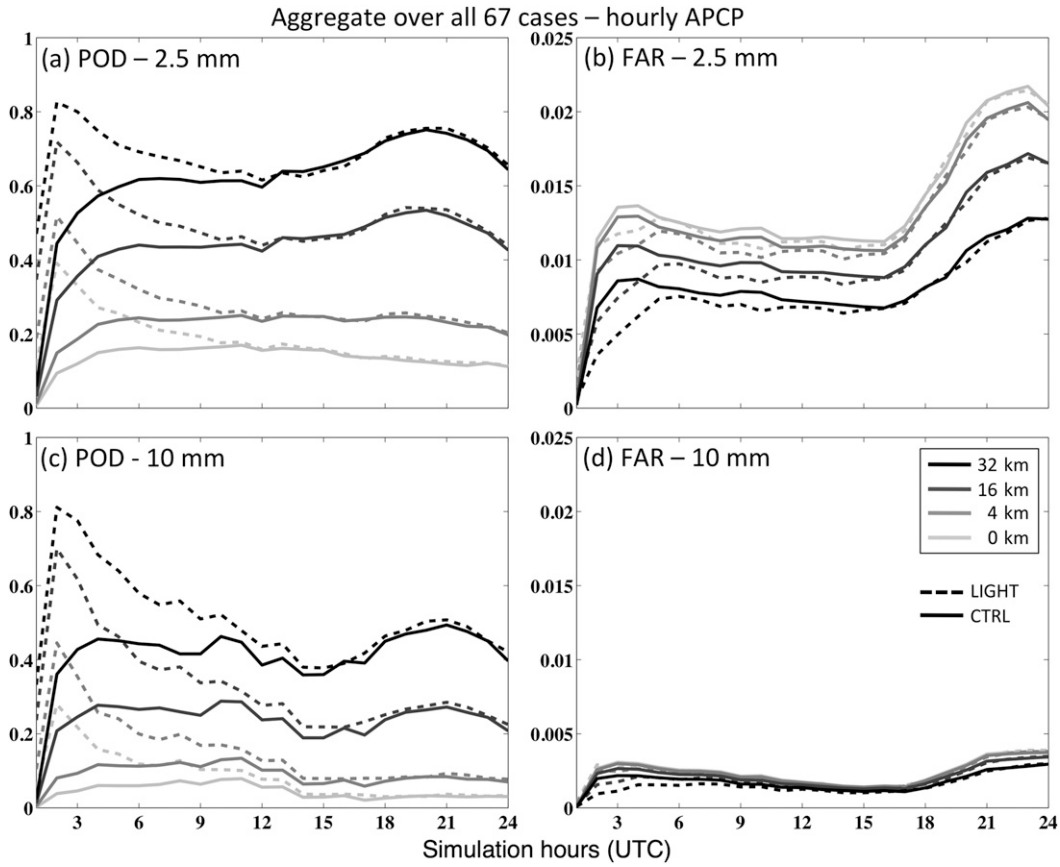

FIG. 11. Probability of detection (POD) of the bias-corrected aggregate contingency data for hourly APCP threshold of (a) 2.5 and (c) 10 mm for the four neighborhood radii indicated in the legend in (d). (b),(d) As in (a),(c), but for the false alarm rate (FAR).

the Hazardous Weather Testbed (HWT; Coniglio et al. 2010; Clark et al. 2012) Spring Forecasting Experiment with the model setup being identical to those from the real-time 4-km NSSL-WRF over CONUS (Clark et al. 2010a,b; Kain et al. 2010a,b; Clark et al. 2012). The variable utilized for the evaluation is the conventional accumulated precipitation (APCP). The chief metric used for evaluating the skill of the lightning assimilation scheme is the neighborhood-based equitable threat score (ETS), which reduces the occurrences of double penalties. Since high biases tend to artificially inflate ETS values, a correction algorithm toward a bias of 1 (perfect forecast) was applied on all the individual cases for each of the six APCP thresholds, nine neighborhood radii, and five APCP periods considered herein (Baldwin and Kain 2006) to yield a bias-corrected ETS (BC-ETS). Last, to determine whether the computed BC-ETS differences between LIGHT and CTRL were statistically significant, a bootstrap resampling technique following Hamill (1999) was applied on the contingency elements for each of the 67 cases examined in this study.

Overall, the results highlight the promising benefit of the routine assimilation of total lightning data toward improving short-term (~6 h) forecasts of high-impact weather events, particularly given its low computational cost and straightforward implementation. Although of lesser magnitude, the BC-ETS differences between LIGHT and CTRL showed that, overall, the improvement from assimilating total lightning could carry up to 12 h of simulation for higher APCP threshold (i.e., ≥10 mm) and accumulation intervals (≥6 h). Similar results were obtained through the fraction skill score (FSS) neighborhood approach.

It is relevant to note, however, that despite these noteworthy improvements, the lightning assimilation scheme produces a noticeable wet bias in the simulated APCP (the rainfall is overpredicted) relative to CTRL. While the amount of water substance mass added by the lightning assimilation is an order of magnitude smaller than the water mass added by the cloud analysis within the 3DVAR code used in F14 for the 29 June 2012 case, potential causes for the high bias in this study could arise

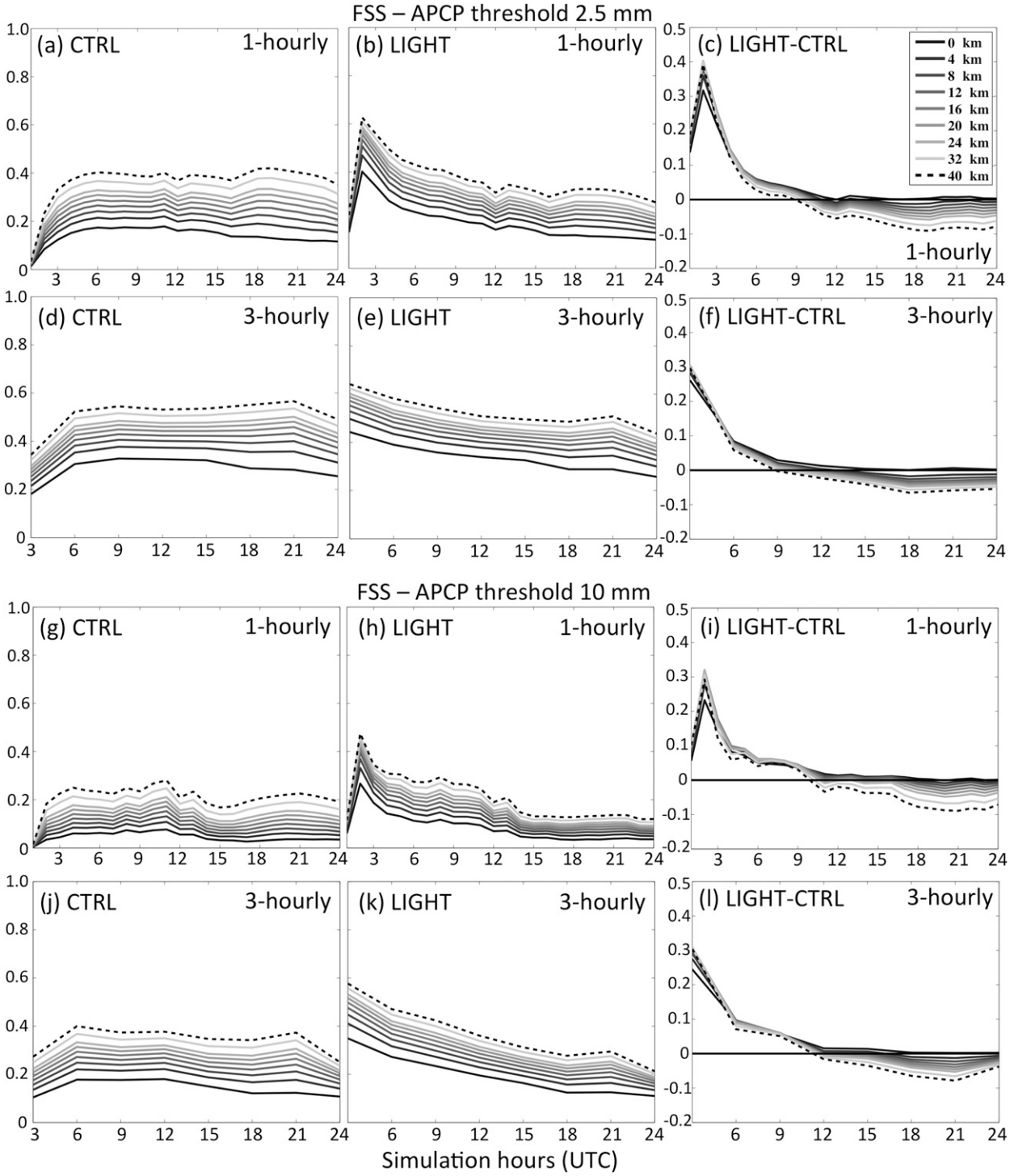

FIG. 12. As in Fig. 8, but for the aggregate (over all 67 cases) fraction skill score (FSS) as defined by Roberts and Lean (2008) for the neighborhood radii indicated in the legend in (c). Note that the ETS employs disks as neighborhood area while the FSS utilizes squares. Thus, the neighborhood radius for FSS should be interpreted with this difference in mind. (a) FSS for 1-h APCP and a threshold of 2.5 mm for CTRL. (b),(c) As in (a), but for LIGHT and the difference between LIGHT and CTRL, respectively. (d)–(f) As in (a)–(c), but for 3-h APCP; (g)–(i) as in (a)–(c), but for 10-mm threshold; and (j)–(l) as in (d)–(f), but for the 10-mm threshold.

from the lightning assimilation scheme still introducing a large amount of moisture in the model (increase of 0.5% of total water substance mass) coupled with errors in the microphysics and the relatively coarse grid spacing employed herein. Because a similarly high positive bias also was produced in the 3DVAR experiments in F14 (not shown), it is likely that the addition of water mass substance in a model already suffering from a positive bias in APCP without any assimilation (as evidenced for instance in Fig. 7a and Figs. 5e–h for CTRL) can only amplify this phenomenon since, eventually, some fraction of this added water mass will be converted to surface precipitation through microphysical processes. As stated earlier, the difference in bias between LIGHT and CTRL could likely be improved by reducing the impact of the assimilation through (i) a shorter assimilation period and/or (ii) by reducing the absolute amount of water vapor mass added per time step, and/or (iii) by adding moisture over a shallower layer.

Also, the improvements incurred by the assimilation of lightning data, as measured by the positive BC-ETS and FSS differences between LIGHT and CTRL, progressively decreased to statistically insignificant (near 0) values past 12 h. This indicated that regardless of the method employed herein to initially place the convective features at the correct locations during the assimilation period, errors in the large-scale fields in the initial conditions will progressively force the solutions of LIGHT to converge to that of CTRL. Moreover, as indicated in F12 and F14 and akin to all lightning nudging methods or cloud analysis schemes published until present, the development of spurious convection is not addressed. This would result in further degrading the forecast through modification of the local environment (e.g., cold pools). Although more computationally expensive, ensemble Kalman filter methods can address the problem of spurious convection [by assimilating zero lightning; Mansell (2014)] and, thus, provide a future alternative pathway to routinely assimilate lightning data.

To reduce the potential moisture bias introduced by the lightning assimilation scheme, the algorithm could be modified to combine heating (e.g., as in Marchand and Fuelberg 2014) with moistening to provide similar buoyancy with less added vapor. F12 proposed a method to partially address the problem of spurious convection, whereby simulated hydrometeor mixing ratios are nudged toward zero at locations where no lightning is observed and where spurious convection develops in the model. This succinct concept was recently tested in a study from Lynn et al. (2015) and revealed improvement of their forecasts. Additional improvements of the lightning assimilation scheme could consider shifting the nudging region downward within the lower troposphere (i.e., toward the cloud base) instead of the mixed-phase region to allow the forced convection to become rooted more quickly in the boundary layer and, incidentally, to also better represent weakly forced, deep convection.

Although there still exists room for improvement, this lightning assimilation scheme has the chief advantage of being computationally inexpensive and easy to port to any numerical weather prediction codes. The capability of readily assimilating lightning data is desirable given that, in contrast to conventionally assimilated weather surveillance radar data, lightning does not suffer from paucity in mountainous areas and oceans. Akin to coarser-resolution satellite data, lightning thus remains a valuable complement to radar data in these regions.

Acknowledgments. The authors thank Bill Callahan, Benny Chukrun, Stan Heckman, and Jim Anderson from Earth Networks for providing the total lightning data. Thanks also goes out to Brett Morrow and Steve Fletcher at NSSL for providing critical IT support toward the completion of the real-time simulations and the subsequent analysis of the data. The Earth Networks lightning data were interpolated onto the local domain in real time using software developed by Dr. Lakshmanan Valliappa. Funding was provided by the NOAA/Office of Oceanic and Atmospheric Research under NOAA–University of Oklahoma Cooperative Agreement NA11OAR4320072, U.S. Department of Commerce. This work was further supported by the National Oceanic and Atmospheric Administration of the U.S. Department of Commerce under Grant NOAA-NESDIS-OAR-NA08OAR4320904 and Grant NOAA-OAR-CIPO-2014-2003893. Auxiliary computer resources were provided by the Oklahoma Supercomputing Center for Education and Research (OSCER) hosted at the University of Oklahoma. Last, the authors also would like to express their gratitude to Jack Kain, three anonymous reviewers, and the editor of *Monthly Weather Review*, Altug Aksoy, for providing valuable comments that helped improve the quality of this manuscript.

REFERENCES

Aksoy, A., D. C. Dowell, and C. Snyder, 2009: A multicase comparative assessment of the ensemble Kalman filter for assimilation of radar observations. Part I: Storm-scale analyses. *Mon. Wea. Rev.,* **137,** 1805–1824, doi:10.1175/2008MWR2691.1.

Alexander, G. D., J. A. Weinman, V. Karyampudi, W. S. Olson, and A. C. L. Lee, 1999: The effect of assimilating rain rates derived from satellites and lightning on forecasts of the 1993 Superstorm. *Mon. Wea. Rev.,* **127,** 1433–1457, doi:10.1175/1520-0493(1999)127<1433:TEOARR>2.0.CO;2.

Baldauf, M., A. Seifert, J. Förstner, D. Majewski, M. Raschendorfer, and T. Reinhardt, 2011: Operational convective-scale numerical weather prediction with the COSMO model: Description

and sensitivities. *Mon. Wea. Rev.,* **139,** 3887–3905, doi:10.1175/MWR-D-10-05013.1.

Baldwin, M. E., and K. E. Mitchell, 1997: The NCEP hourly multisensor U.S. precipitation analysis for operations and GCIP research. Preprints, *13th Conf. on Hydrology,* Long Beach, CA, Amer. Meteor. Soc., 54–55.

——, and J. S. Kain, 2006: Sensitivity of several performance measures to displacement error, bias, and event frequency. *Wea. Forecasting,* **21,** 636–648, doi:10.1175/WAF933.1.

Benjamin, S. G., and Coauthors, 2004: An hourly assimilation–forecast cycle: The RUC. *Mon. Wea. Rev.,* **132,** 495–518, doi:10.1175/1520-0493(2004)132<0495:AHACTR>2.0.CO;2.

Boccippio, D. J., K. L. Cummins, H. J. Christian, and S. J. Goodman, 2001: Combined satellite- and surface-based estimation of the intracloud–cloud-to-ground lightning ratio over the continental United States. *Mon. Wea. Rev.,* **129,** 108–122, doi:10.1175/1520-0493(2001)129<0108:CSASBE>2.0.CO;2.

Bruning, E. C., W. D. Rust, D. R. MacGorman, M. I. Biggerstaff, and T. J. Schuur, 2010: Formation of charge structures in a supercell. *Mon. Wea. Rev.,* **138,** 3740–3761, doi:10.1175/2010MWR3160.1.

Bryan, G. H., J. C. Wyngaard, and J. M. Fritsch, 2003: Resolution requirements for the simulation of deep moist convection. *Mon. Wea. Rev.,* **131,** 2394–2416, doi:10.1175/1520-0493(2003)131<2394:RRFTSO>2.0.CO;2.

Casati, B., and Coauthors, 2008: Forecast verification: Current status and future directions. *Meteor. Appl.,* **15,** 3–18, doi:10.1002/met.52.

Chang, D.-E., J. A. Weinman, C. A. Morales, and W. S. Olson, 2001: The effect of spaceborne microwave and ground-based continuous lightning measurements on forecasts of the 1998 Groundhog Day storm. *Mon. Wea. Rev.,* **129,** 1809–1833, doi:10.1175/1520-0493(2001)129<1809:TEOSMA>2.0.CO;2.

Chen, F., and J. Dudhia, 2001: Coupling an advanced land surface–hydrology model with the Penn State–NCAR MM5 modeling system. Part I: Model implementation and sensitivity. *Mon. Wea. Rev.,* **129,** 569–585, doi:10.1175/1520-0493(2001)129<0569:CAALSH>2.0.CO;2.

——, Z. Janjic, and K. Mitchell, 1997: Impact of atmospheric surface-layer parameterizations in the new land-surface scheme of the NCEP mesoscale Eta Model. *Bound.-Layer Meteor.,* **85,** 391–421, doi:10.1023/A:1000531001463.

Clark, A. J., W. A. Gallus, and T. C. Chen, 2007: Comparison of the diurnal precipitation cycle in convection-resolving and non-convection-resolving mesoscale models. *Mon. Wea. Rev.,* **135,** 3456–3473, doi:10.1175/MWR3467.1.

——, ——, M. Xue, and F. Kong, 2010a: Convection-allowing and convection-parameterizing ensemble forecasts of a mesoscale convective vortex and associated severe weather environment. *Wea. Forecasting,* **25,** 1052–1081, doi:10.1175/2010WAF2222390.1.

——, ——, and M. L. Weisman, 2010b: Neighborhood-based verification of precipitation forecasts from convection-allowing NCAR WRF Model simulations and the operational NAM. *Wea. Forecasting,* **25,** 1495–1509, doi:10.1175/2010WAF2222404.1.

——, and Coauthors, 2012: An overview of the 2010 Hazardous Weather Testbed Experimental Forecast Program Spring Experiment. *Bull. Amer. Meteor. Soc.,* **93,** 55–74, doi:10.1175/BAMS-D-11-00040.1.

Coniglio, M. C., K. L. Elmore, J. S. Kain, S. J. Weiss, M. Xue, and M. L. Weisman, 2010: Evaluation of WRF model output for severe weather forecasting from the 2008 NOAA Hazardous Weather Testbed Spring Experiment. *Wea. Forecasting,* **25,** 408–427, doi:10.1175/2009WAF2222258.1.

Deierling, W., and W. A. Petersen, 2008: Total lightning activity as an indicator of updraft characteristics. *J. Geophys. Res.,* **113,** D16210, doi:10.1029/2007JD009598.

Dixon, M., Z. Li, H. Lean, N. Roberts, and S. Ballard, 2009: Impact of data assimilation on forecasting convection over the United Kingdom using a high-resolution version of the Met Office Unified Model. *Mon. Wea. Rev.,* **137,** 1562–1584, doi:10.1175/2008MWR2561.1.

Done, J., C. Davis, and M. Weisman, 2004: The next generation of NWP: Explicit forecasts of convection using the Weather Research and Forecasting (WRF) model. *Atmos. Sci. Lett.,* **5,** 110–117, doi:10.1002/asl.72.

Dudhia, J., 1989: Numerical study of convection observed during the winter monsoon experiment using a mesoscale two-dimensional model. *J. Atmos. Sci.,* **46,** 3077–3107, doi:10.1175/1520-0469(1989)046<3077:NSOCOD>2.0.CO;2.

Ebert, E. E., 2009: Neighborhood verification: A strategy for rewarding close forecasts. *Wea. Forecasting,* **24,** 1498–1510, doi:10.1175/2009WAF2222251.1.

Ek, M. B., K. E. Mitchell, Y. Lin, E. Rogers, P. Grunmann, V. Koren, G. Gayno, and J. D. Tarpley, 2003: Implementation of Noah land surface model advances in the National Centers for Environmental Prediction operational mesoscale Eta Model. *J. Geophys. Res.,* **108,** 8851, doi:10.1029/2002JD003296.

Emersic, C., and C. P. R. Saunders, 2010: Further laboratory investigations into the relative diffusional growth rate theory of thunderstorm electrification. *Atmos. Res.,* **98,** 327–340, doi:10.1016/j.atmosres.2010.07.011.

Evensen, G., 1994: Sequential data assimilation with a nonlinear quasi-geostrophic model using Monte Carlo methods to forecast error statistics. *J. Geophys. Res.,* **99,** 10 143–10 162, doi:10.1029/94JC00572.

——, 2003: The ensemble Kalman filter: Theoretical formulation and practical implementation. *Ocean Dyn.,* **53,** 343–367, doi:10.1007/s10236-003-0036-9.

Fierro, A. O., M. S. Gilmore, E. R. Mansell, L. J. Wicker, and J. M. Straka, 2006: Electrification and lightning in an idealized boundary-crossing supercell simulation of 2 June 1995. *Mon. Wea. Rev.,* **134,** 3149–3172, doi:10.1175/MWR3231.1.

——, R. F. Rogers, F. D. Marks, and D. S. Nolan, 2009: The impact of horizontal grid spacing on the microphysical and kinematic structures of strong tropical cyclones simulated with the WRF-ARW model. *Mon. Wea. Rev.,* **137,** 3717–3743, doi:10.1175/2009MWR2946.1.

——, X.-M. Shao, T. Hamlin, J. M. Reisner, and J. Harlin, 2011: Evolution of eyewall convective events as indicated by intracloud and cloud-to-ground lightning activity during the rapid intensification of Hurricanes Rita and Katrina. *Mon. Wea. Rev.,* **139,** 1492–1504, doi:10.1175/2010MWR3532.1.

——, E. R. Mansell, C. Ziegler, and D. R. MacGorman, 2012: Application of a lightning data assimilation technique in the WRF-ARW Model at cloud-resolving scales for the tornado outbreak of 24 May 2011. *Mon. Wea. Rev.,* **140,** 2609–2627, doi:10.1175/MWR-D-11-00299.1.

——, ——, ——, and ——, 2013: The implementation of an explicit charging and discharge lightning scheme within the WRF-ARW Model: Benchmark simulations of a continental squall line, a tropical cyclone, and a winter storm. *Mon. Wea. Rev.,* **141,** 2390–2415, doi:10.1175/MWR-D-12-00278.1.

——, J. Gao, C. L. Ziegler, E. R. Mansell, D. R. MacGorman, and S. R. Dembek, 2014: Evaluation of a cloud-scale lightning data assimilation technique and a 3DVAR method for the analysis and short-term forecast of the 29 June 2012

derecho event. *Mon. Wea. Rev.,* **142,** 183–202, doi:10.1175/MWR-D-13-00142.1.

Fritsch, J. M., and C. F. Chappell, 1981: Preliminary numerical tests of the modification of mesoscale convective systems. *J. Appl. Meteor.,* **20,** 910–921, doi:10.1175/1520-0450(1981)020<0910:PNTOTM>2.0.CO;2.

——, R. J. Kain, and C. R. Chelius, 1986: The contribution of mesoscale convective weather systems to the warm-season precipitation in the United States. *J. Climate Appl. Meteor.,* **25,** 1333–1345, doi:10.1175/1520-0450(1986)025<1333:TCOMCW>2.0.CO;2.

Gao, J., and D. J. Stensrud, 2012: Assimilation of reflectivity data in a convective-scale, cycled 3DVAR framework with hydrometeor classification. *J. Atmos. Sci.,* **69,** 1054–1065, doi:10.1175/JAS-D-11-0162.1.

——, and Coauthors, 2013: A real-time weather-adaptive 3DVAR analysis system for severe weather detections and warnings. *Wea. Forecasting,* **28,** 727–745, doi:10.1175/WAF-D-12-00093.1.

Godinez, H. C., J. M. Reisner, A. O. Fierro, S. R. Guimond, and J. Kao, 2012: Determining key model parameters of rapidly intensifying Hurricane Guillermo (1997) using the ensemble Kalman filter. *J. Atmos. Sci.,* **69,** 3147–3171, doi:10.1175/JAS-D-12-022.1.

Goodman, S. J., and D. R. MacGorman, 1986: Cloud-to-ground lightning activity in mesoscale convective complexes. *Mon. Wea. Rev.,* **114,** 2320–2328, doi:10.1175/1520-0493(1986)114<2320:CTGLAI>2.0.CO;2.

——, and Coauthors, 2012: The GOES-R proving ground: Accelerating user readiness for the next-generation geostationary environmental satellite system. *Bull. Amer. Meteor. Soc.,* **93,** 1029–1040, doi:10.1175/BAMS-D-11-00175.1.

——, and Coauthors, 2013: The GOES-R Geostationary Lightning Mapper (GLM). *Atmos. Res.,* **125–126,** 34–49, doi:10.1016/j.atmosres.2013.01.006.

Grams, J. S., W. A. Gallus, S. E. Koch, L. S. Wharton, A. Loughe, and E. E. Ebert, 2006: The use of a modified Ebert–McBride technique to evaluate mesoscale model QPF as a function of convective system morphology during IHOP 2002. *Wea. Forecasting,* **21,** 288–306, doi:10.1175/WAF918.1.

Gurka, J. J., T. A. Schmit, T. M. Renkevens, M. M. Gunshor, and J. Li, 2006: Update on baseline instruments for GOES-R series. *Atmospheric and Environmental Remote Sensing Data Processing and Utilization II: Perspective on Calibration/Validation Initiatives and Strategies,* A. H. L. Huang and H. J. Bloom, Eds., International Society for Optical Engineering (SPIE Proceedings, Vol. 6301), 63010H, doi:10.1117/12.683701.

Hamill, T. M., 1999: Hypothesis tests for evaluating numerical precipitation forecasts. *Wea. Forecasting,* **14,** 155–167, doi:10.1175/1520-0434(1999)014<0155:HTFENP>2.0.CO;2.

Hong, S.-Y., and J.-O. J. Lim, 2006: The WRF single-moment microphysics scheme (WSM6). *J. Korean Meteor. Soc.,* **42,** 129–151.

Houtekamer, P. L., and H. Mitchell, 1998: Data assimilation using an ensemble Kalman filter technique. *Mon. Wea. Rev.,* **126,** 796–811, doi:10.1175/1520-0493(1998)126<0796:DAUAEK>2.0.CO;2.

Hu, M., M. Xue, and K. Brewster, 2006: 3DVAR and cloud analysis with WSR-88D level-II data for the prediction of the Fort Worth, Texas, tornadic thunderstorms. Part I: Cloud analysis and its impact. *Mon. Wea. Rev.,* **134,** 675–698, doi:10.1175/MWR3092.1.

Ikeda, K., M. Steiner, J. Pinto, and C. Alexander, 2013: Evaluation of cold-season precipitation forecasts generated by the hourly updating high-resolution rapid refresh model. *Wea. Forecasting,* **28,** 921–939, doi:10.1175/WAF-D-12-00085.1.

Janjic, Z. I., 1994: The step-mountain eta coordinate model: Further developments of the convection, viscous sublayer, and turbulence closure schemes. *Mon. Wea. Rev.,* **122,** 927–945, doi:10.1175/1520-0493(1994)122<0927:TSMECM>2.0.CO;2.

Jenkner, J., C. Frei, and C. Schwierz, 2008: Quantile-based short-range QPF evaluation over Switzerland. *Meteor. Z.,* **17,** 827–848, doi:10.1127/0941-2948/2008/0344.

Jones, T. A., J. A. Otkin, D. J. Stensrud, and K. Knopfmeier, 2014: Forecast evaluation of an observing system simulation experiment assimilating both radar and satellite data. *Mon. Wea. Rev.,* **142,** 107–124, doi:10.1175/MWR-D-13-00151.1.

Kain, J. S., S. J. Weiss, J. J. Levit, M. E. Baldwin, and D. R. Bright, 2006: Examination of convection-allowing configurations of the WRF Model for the prediction of severe convective weather: The SPC/NSSL Spring Program 2004. *Wea. Forecasting,* **21,** 167–181, doi:10.1175/WAF906.1.

——, and Coauthors, 2008: Some practical considerations regarding horizontal resolution in the first generation of operational convection-allowing NWP. *Wea. Forecasting,* **23,** 931–952, doi:10.1175/WAF2007106.1.

——, and Coauthors, 2010a: Assessing advances in the assimilation of radar data and other mesoscale observations within a collaborative forecasting–research environment. *Wea. Forecasting,* **25,** 1510–1521, doi:10.1175/2010WAF2222405.1.

——, S. R. Dembek, S. J. Weiss, J. L. Case, J. J. Levit, and R. A. Sobash, 2010b: Extracting unique information from high-resolution forecast models: Monitoring selected fields and phenomena every time step. *Wea. Forecasting,* **25,** 1536–1542, doi:10.1175/2010WAF2222430.1.

——, and Coauthors, 2013: A feasibility study for probabilistic convection initiation forecasts based on explicit numerical guidance. *Bull. Amer. Meteor. Soc.,* **94,** 1213–1225, doi:10.1175/BAMS-D-11-00264.1.

Lynn, B. H., G. Kelman, and G. Ellrod, 2015: An evaluation of the efficacy of using observed lightning to improve convective lightning forecasts. *Wea. Forecasting,* doi:10.1175/WAF-D-13-00028.1, in press.

MacGorman, D. R., D. W. Burgess, V. Mazur, W. D. Rust, W. L. Taylor, and B. C. Johnson, 1989: Lightning rates relative to tornadic storm evolution on 22 May 1981. *J. Atmos. Sci.,* **46,** 221–251, doi:10.1175/1520-0469(1989)046<0221:LRRTTS>2.0.CO;2.

Maddox, R. A., 1980: Meoscale convective complexes. *Bull. Amer. Meteor. Soc.,* **61,** 1374–1387, doi:10.1175/1520-0477(1980)061<1374:MCC>2.0.CO;2.

Mansell, E. R., 2014: Storm-scale ensemble Kalman filter assimilation of total lightning flash data. *Mon. Wea. Rev.,* **142,** 3683–3695, doi:10.1175/MWR-D-14-00061.1.

——, C. L. Ziegler, and D. R. MacGorman, 2007: A lightning data assimilation technique for mesoscale forecast models. *Mon. Wea. Rev.,* **135,** 1732–1748, doi:10.1175/MWR3387.1.

Marchand, M., and H. Fuelberg, 2014: Assimilation of lightning data using a nudging method involving low-level warming. *Mon. Wea. Rev.,* **142,** 4850–4871, doi:10.1175/MWR-D-14-00076.1.

Mellor, G. L., and T. Yamada, 1982: Development of turbulence closure model for geophysical fluid problems. *Rev. Geophys. Space Phys.,* **20,** 851–875, doi:10.1029/RG020i004p00851.

Mesinger, F., 2008: Bias adjusted precipitation threat scores. *Adv. Geosci.,* **16,** 137–142, doi:10.5194/adgeo-16-137-2008.

Mlawer, E., S. Taubman, P. Brown, M. Iacono, and S. Clough, 1997: Radiative transfer for inhomogeneous atmospheres: RRTM, a validated correlated-k model for the longwave. *J. Geophys. Res.,* **102,** 16 663–16 682, doi:10.1029/97JD00237.

Papadopoulos, A., T. G. Chronis, and E. N. Anagnostou, 2005: Improving convective precipitation forecasting through

assimilation of regional lightning measurements in a mesoscale model. *Mon. Wea. Rev.,* **133,** 1961–1977, doi:10.1175/MWR2957.1.

Pessi, A. T., and S. Businger, 2009: The impact of lightning data assimilation on a winter storm simulation over the North Pacific Ocean. *Mon. Wea. Rev.,* **137,** 3177–3195, doi:10.1175/2009MWR2765.1.

Roberts, N. M., 2005: An investigation of the ability of a storm scale configuration of the Met Office NWP model to predict flood-producing rainfall. Met Office Tech. Rep. 455, 80 pp.

——, and H. W. Lean, 2008: Scale-selective verification of rainfall accumulations from high-resolution forecasts of convective events. *Mon. Wea. Rev.,* **136,** 78–97, doi:10.1175/2007MWR2123.1.

Saunders, C. P. R., and L. S. Peck, 1998: Laboratory studies of the influence of the rime accretion rate on charge transfer during crystal/graupel collisions. *J. Geophys. Res.,* **103,** 13 949–13 956, doi:10.1029/97JD02644.

Schwartz, C. S., and Coauthors, 2010: Toward improved convection-allowing ensembles: Model physics sensitivities and optimizing probabilistic guidance with small ensemble membership. *Wea. Forecasting,* **25,** 263–280, doi:10.1175/2009WAF2222267.1.

Skamarock, W. C., 2004: Evaluating mesoscale NWP models using kinetic energy spectra. *Mon. Wea. Rev.,* **132,** 3019–3032, doi:10.1175/MWR2830.1.

——, and J. B. Klemp, 2008: A time-split nonhydrostatic atmospheric model for weather research and forecasting applications. *J. Comput. Phys.,* **227,** 3465–3485, doi:10.1016/j.jcp.2007.01.037.

Stensrud, D. J., and Coauthors, 2009: Convective-scale Warn-On-Forecast system: A vision for 2020. *Bull. Amer. Meteor. Soc.,* **90,** 1487–1499, doi:10.1175/2009BAMS2795.1.

Sugimoto, S., D. M. Barker, N. A. Crook, J. Sun, and Q. Xiao, 2009: An examination of WRF 3DVAR data assimilation on its capabilities in retrieving unobserved variables and forecasting precipitation through observing system simulation experiments. *Mon. Wea. Rev.,* **137,** 4011–4029, doi:10.1175/2009MWR2839.1.

Takahashi, T., 1978: Riming electrification as a charge generation mechanism in thunderstorms. *J. Atmos. Sci.,* **35,** 1536–1548, doi:10.1175/1520-0469(1978)035<1536:REAACG>2.0.CO;2.

Wang, S. Y., T. C. Chen, and S. E. Taylor, 2009: Evaluations of NAM forecasts on midtropospheric perturbation-induced convective storms over the U.S. northern plains. *Wea. Forecasting,* **24,** 1309–1333, doi:10.1175/2009WAF2222185.1.

Weisman, M. L., C. Davis, W. Wang, K. W. Manning, and J. B. Klemp, 2008: Experiences with 0–36 h explicit convective forecasts with the WRF-ARW model. *Wea. Forecasting,* **23,** 407–437, doi:10.1175/2007WAF2007005.1.

Wiens, K. C., S. A. Rutledge, and S. A. Tessendorf, 2005: The 29 June 2000 supercell observed during STEPS. Part II: Lightning and charge structure. *J. Atmos. Sci.,* **62,** 4151–4177, doi:10.1175/JAS3615.1.

Zhang, F., Y. Weng, J. A. Sippel, Z. Meng, and C. H. Bishop, 2009: Cloud-resolving hurricane initialization and prediction through assimilation of Doppler radar observations with an ensemble Kalman filter. *Mon. Wea. Rev.,* **137,** 2105–2125, doi:10.1175/2009MWR2645.1.